On the surface energy balance closure at different temporal scales

On the surface energy balance closure at different temporal scales

Andrey A. Grachev [a, b, *], **Christopher W. Fairall** [a], **Byron W. Blomquist** [a, b], **Harindra J. S. Fernando** [c], **Laura S. Leo** [c], **Sebastián F. Otárola-Bustos** [c], **James M. Wilczak** [a], **Katherine L. McCaffrey** [a, b, 1]

[a] NOAA Earth System Research Laboratory, 325 Broadway, R/PSD3, Boulder, CO 80305-3337, USA

[b] Cooperative Institute for Research in Environmental Sciences, University of Colorado, Boulder, CO, USA

[c] Department of Civil & Environmental Engineering & Earth Sciences, University of Notre Dame, Notre Dame, IN, USA

[*] *Corresponding author. E-mail address*: Andrey.Grachev@noaa.gov (Andrey A. Grachev)

[1] Now at: S & P Global Market Intelligence, Boulder, CO, USA

Agricultural and Forest Meteorology

AGRFORMET-D-19-00569

Manuscript submitted: 25 May 2019
Major Revisions: 14 September 2019
Minor Revisions: 18 October 2019

Abstract

Measurements of the surface energy fluxes (turbulent and radiative) and other ancillary atmospheric/soil parameters made in the Columbia River Basin (Oregon) in an area of complex terrain during a 10-month long portion of the second Wind Forecast Improvement Project (WFIP 2) field campaign are used to study the surface energy budget (SEB) and surface fluxes over different temporal scales. This study analyzes and discusses SEB closure based on half-hourly, daily, monthly, seasonal, and sub-annual (~10-month) temporal averages. The data were collected over all four seasons for different states of the underlying ground surface (dry, wet, and frozen). Our half-hourly direct measurements of energy balance show that the sum of the turbulent sensible and latent heat fluxes systematically underestimate positive net radiation by around 20-30% during daytime and overestimate negative net radiation at night. This imbalance of the surface energy budget is comparable to other terrestrial sites. However, on average, the residual energy imbalance is significantly reduced at daily, weekly, and monthly averaging timescales, and moreover, the SEB can be closed for this site within reasonable limits on seasonal and sub-annual timescales (311-day averaging for the entire field campaign dataset). Increasing the averaging time to daily and longer time intervals substantially reduces the ground heat flux and storage terms, because energy locally entering the soil, air column, and vegetation in the morning is released in the afternoon and evening. Averaging on daily to sub-annual timescales also reduces random instrumental measurement errors and other uncertainties as well as smooths out a hysteresis effect (phase lag) in the SEB relationship between different components. This study shows that SEB closure is better for dry soils compared to wet soils and the statistical dependence of the turbulent fluxes and net radiation for freezing soil surfaces

appears weak, if not non-existent, apparently due to lack of the latent heat of fusion term in the traditional SEB equation.

Keywords: Energy balance closure • Radiative fluxes • Surface energy budget • Time averaging • Turbulent fluxes

1. Preamble

Surface energy fluxes (turbulent, radiative, and ground heat) are important in a wide variety of applications including climate modelling, weather forecasting, land-atmosphere simulations, agricultural and forestry research, and environmental impact studies. A direct application of the surface energy fluxes is the net surface energy budget (SEB). Energy balance closure including all components of the SEB at the air-surface interface is necessary for a better understanding of the atmosphere-surface exchange mechanisms and to improve models over representative areas and yearly timescales.

Surface energy balance closure is a formulation of the conservation of energy principle (the first law of thermodynamics). In other words, the SEB equation is a statement of how the net radiation is balanced by turbulent sensible, latent, and soil heat fluxes in the absence of other energy sources and sinks. Comprehensive SEB studies have been conducted since the 1950-60s (e.g., Lettau and Davidson 1957; Long et al. 1964). Since the late 1980s, it has become obvious that the surface energy balance is difficult to close at temporal scales less than several hours (e.g., at half-hourly and hourly averaged time scales) as reported in many studies (e.g., Wilson et al. 2002; Foken et al. 2006; Mauder et al. 2007; Oncley et al. 2007; Cava et al. 2008; Foken 2008; Jacobs et al. 2008; Panin and Bernhofer 2008; Higgins 2012; Leuning et al. 2012; Stoy et al. 2013; Cuxart et al. 2015; Majozi et al. 2017; Gao et al. 2017a and references therein). According to field measurements, the sum of the turbulent fluxes of sensible and latent heat plus the ground heat flux in most cases (generally during daytime) is systematically smaller than that required to balance the net radiation; whereas this sum generally overestimate the net radiation at night. The lack of energy balance closure at half-hourly and hourly measurements is a

94 fundamental and pervasive problem in micrometeorology. Note, however, that in some cases the
95 authors reported that the energy budget can be closed within reasonable limits (e.g., Lamaud et
96 al. 2001; Jacobs et al. 2008), but these successes are rare.
97 This study utilizes the data of surface fluxes (turbulent and radiative) and other ancillary
98 atmospheric and soil data collected in the Columbia River Gorge area near Wasco, Oregon,
99 during a 10-month long period within the second Wind Forecast Improvement Project (WFIP 2)
100 from 24 June 2016 through 1 May 2017 (year days 176–487 with respect to 1 January 2016). The
101 WFIP 2 project is a four-year multi-disciplinary effort intended to improve short-term weather
102 forecast models and better understand various unresolved physical processes that affect wind
103 energy generation in regions of complex terrain such as coastlines, mountains, and canyons, in
104 order to develop and evaluate improved surface-flux parameterizations (see Bianco et al. 2019;
105 Olson et al. 2019; Shaw et al. 2019; Wilczak et al. 2019 for details). The observational phase of
106 the WFIP 2 allows for an analysis of the SEB for different soils over a broad range of temporal
107 scales based on first principles.
108 The main objectives of this study are twofold. The first objective is an investigation of
109 the non-closure of the SEB for three different type of soils (dry, wet, and frozen surfaces) using
110 the same instruments, experimental setup, location, and data processing. The second objective is
111 an analysis of SEB closure at different temporal scales from half-hourly to daily and even
112 monthly, seasonal and sub-annual averaged time series. In some sense, this study bridges
113 micrometeorological measurements and climatological timescales through temporal averaging.
114 The layout of the paper is as follows. The theoretical background (basic SEB equations) and the
115 energy balance closure problem are considered in Section 2. Instruments, data collection and site
116 descriptions are documented in Section 3. Main findings of the study based on analysis of the

117 WFIP 2 experimental data (e.g., time series, SEB at different timescales, and over different types
118 of soil surfaces) are described in Section 4. The conclusions are summarized in Section 5.
119
120 **2. The Surface Energy Balance Closure Problem**
121
122 The law of conservation of energy at the interface between atmosphere and land in the
123 absence of other energy sources and sinks is written as:
124 $$H_S + H_L + G = R_{net} \quad (1)$$
125 where G is the soil heat flux, R_{net} is the net radiation defined as the balance between
126 downwelling (incoming) and upwelling (outgoing) SW and LW radiation:
127 $$R_{net} = SW_{down} - SW_{up} + LW_{down} - LW_{up} \quad (2)$$
128 The turbulent fluxes of sensible heat H_S and latent heat H_L in (1) can be estimated by the eddy
129 correlation method according to
130 $$H_S = c_p \rho \overline{w'\theta'} \quad (3)$$
131 $$H_L = \mathcal{L}_e \rho \overline{w'q'} \quad (4)$$
132 where ρ is the mean air density, θ is the air potential temperature, q is the air specific humidity,
133 c_p is the specific heat capacity of air at constant pressure, and $\mathcal{L}_e$ is the latent heat of evaporation
134 of water. Here w is the vertical velocity component, the prime [$'$] denotes fluctuations about the
135 mean value, and an overbar is an averaging operator (half an hour in this study).
136 As mentioned above, numerous direct measurements of all SEB components in (1) have
137 shown that over land the sum $H_S + H_L + G$ in most cases (generally during daytime)
138 systematically underestimate the net radiation R_{net} by about 20-30% (Foken and Oncley 1995;
139 Wilson et al. 2002; Meyers and Hollinger 2004; Foken et al. 2006; Mauder et al. 2007; Cava et

al. 2008; Foken 2008; Jacobs et al. 2008; Panin and Bernhofer 2008; Higgins 2012; Leuning et al. 2012; Stoy et al. 2013; Masseroni et al. 2014; Gao et al. 2017a).

Because the energy balance at the surface often cannot be closed based on experimental observations, the SEB equation (1) is typically formulated as (e.g., Foken et al. 2006):

$$H_S + H_L + G + Res = R_{net} \quad (5)$$

where Res is any residual term (imbalance). Equation (1) assumes an ideal case, when all the fluxes are measured at the infinitesimal interface between an atmosphere and a soil, while Eq. (5) implies a two-layer (atmosphere and soil) column of finite thickness (e.g., Foken 2008, Fig. 1). The turbulent and soil fluxes in (5) are measured at the upper and lower boundary planes of the total layer respectively. Clearly a variety of factors may be responsible for the lack of SEB closure in the layer (e.g., Foken et al. 2006; Mauder et al. 2007; Higgins 2012; Leuning et al. 2012). Therefore, in general Res can be partitioned as:

$$Res = T + S + X \quad (6)$$

where T is an additional transport (vertical and horizontal) through all boundary planes, S is a total storage in the two-layer column, and X indicates all other unspecified contributions to (1).

The additional transport term T in (6) includes the divergence of the horizontal turbulent flux caused by complex terrain or heterogeneities in the underlying surface and soil heat transfer by convection or circulation (in addition to conductive heat flux G) and/or by convective water flux in the water-saturated soils at the bottom plane (the water flux in the soil is a consequence of the law of conservation of mass in the case $H_L \neq 0$). The storage term, S, can be partitioned as (e.g., Meyers and Hollinger 2004; Oncley et al. 2007; Leuning et al. 2012; Masseroni et al. 2014):

$$S = S_a + S_g + S_p + S_c + S_x \quad (7)$$

Where S_a is storage of energy in the air column due to radiative and/or sensible heat flux divergence (the air enthalpy change), S_g is the ground heat storage above a a heat flux plate measurement level, S_p is the radiation consumed in photosynthesis (the photosynthesis flux), S_c is the canopy heat storage in biomass (the rate change in enthalpy of the vegetation), and S_x is all other storage terms, e.g. the atmospheric moisture change and the canopy dew water enthalpy change (Jacobs et al. 2008). The term X in Eq. (6) may include several factors: loss of low-frequency covariance contributions to the turbulent fluxes induced by insufficient averaging time and/or inadequate resolution of high-frequency flux components; choice of coordinate systems; the mismatch between the footprint of the turbulent heat fluxes and the measurements of radiation components and soil heat fluxes; instrumental errors; the latent heat of fusion term (see below); etc. The lack of SEB closure raises concerns regarding eddy covariance measurements at standard half-hourly and hourly averaging time scales. There are suggestions that increasing the turbulence averaging time can improve SEB closure by capturing additional sensible and latent heat fluxes at low-frequencies (e.g., Foken 2008).

Recall that failure to close the energy balance is associated with a systematic bias. Specifically, for a positive net radiation, $R_{net} > 0$ (generally during daytime), the left-hand side of Eq. (1) is routinely smaller than the right-hand side ($Res > 0$ in Eq. (5)) and vice versa for a negative net radiation, $R_{net} < 0$ (generally during nigh). An immediate problem for the additional terms (6) is that the different terms contribute differently (either positively or negatively) to the bias. While all the storage terms (7) and the loss of high-frequency components in the turbulent fluxes contribute positively to *Res* in the case $R_{net} > 0$, it is difficult to see why the loss of low-frequency covariance associated with local circulations would always lead to an underestimation of the turbulent fluxes, and the same could be said about advection

(Finnigan 2008). For example, according to SHEBA data (Grachev et al. 2005, Fig. 8), the low-frequency flux components can be both positive and negative. Thus, while the storage term S in Eq. (6) is always positive (systematic contribution) for the positive net radiation, the other two terms, T and X, contribute positively or negatively to the bias (random contribution).

The various terms in Eq. (1) differ greatly in magnitude. Generally the soil heat flux G is relatively small compared with the net radiation, but in some cases the G term in Eq. (1) cannot be ignored. Magnitude of the ratio G/R_{net} will typically vary between 0.05 and 0.50, depending on the period of the day, thermal properties of the soil, surface cover, soil moisture content, and solar irradiance (Kustas et al. 1993). For example, midday values of the ratio of the soil heat flux and the net radiation, G/R_{net}, are about 0.15 for measurements over fields of bare soil, alfalfa, and cotton near Phoenix, AZ according to Kustas and Daughtry (1990), and 0.14-0.17 for a no-till cornfield in central Iowa in November (Sauer et al. 1998). During the night or in the fall/winter, G is an important term in (1), when R_{net} is low and stable atmospheric conditions cause H_S and H_L to be small. Despite its relative importance, the soil heat flux is not often measured, including this study where the observational site was not instrumented with a heat flux plate (e.g., see survey in Liebethal et al. 2005; Liebethal and Foken 2007; Gao et al. 2017b; Yang and Wang 2008).

The soil heat flux can be estimated from soil temperature profile measurements using Fourier's Law of Heat Conduction (gradient method)

$$G(z) = -\lambda \frac{\partial T_S}{\partial z} \tag{8}$$

where λ is the thermal conductivity of the soil and $\partial T_S/\partial z$ is the vertical temperature gradient of the soil temperature, T_S. In practical applications the first derivative of the soil temperature in (8) is usually replaced by the finite-difference approximation in the soil layer Δz and Eq. (8) reduces

209 to $G(z) \approx -\lambda \Delta T_S / \Delta z$. Fourier's Law (8) presumes steady state heat conduction, one-dimensional
210 heat flow, an isotropic and homogeneous material, constant thermal conductivity λ, and no
211 internal heat generation. Generally, soil is a three-phase material (water, air, solid) and
212 application of Eq. (8) is considerably more difficult. The thermal conductivity of soil depends on
213 the conductivity of each phase and their proportions; that is, λ varies by composition of the solid
214 fraction (e.g., mineral type and particle size), water content (thermal conductivity of water is
215 about two to three times greater than that of soil), amount of organic matter, and bulk density. As
216 a result, λ values can change between layers within Δz even for the same soil due to changes in
217 water content. Another complexity of the gradient method (8) is associated with non-stationarity
218 (diurnal variations), even during a half-hour averaging period. The diurnal cycle of solar
219 radiation modulates a sinusoidal variation in the ground surface heat flux and diurnal thermal
220 waves in the top soil layer. The temperature wave damps exponentially with depth and its lag
221 time increases with depth. The ground heat flux is theoretically $\pi/4$ (1/8 cycle) out of phase with
222 the temperature wave (hysteresis effect); that is, the ground heat flux is largest three hours ahead
223 of the surface temperature for a diurnally varying surface temperature cycle (Arya 1988; Garratt
224 1992; Gao et al. 2010). Thus, while the gradient method (8) is simple to employ under field
225 conditions, accurate measurement of λ and the vertical soil temperature gradient is challenging.
226 The impact of the hysteresis effect in diurnal cycles and the effect of the wave phase difference
227 between different atmospheric and/or soil variables on the SEB closure are discussed in number
228 of studies (e.g., Gao et al. 2010, 2017a; Sun et al. 2013).

229 Direct measurements of the turbulent flux of carbon dioxide allow estimation of a storage
230 term S_p in (7) associated with the photosynthesis flux. The photosynthesis flux S_p is the change
231 in the Gibbs free energy and, according to Nobel (2009, Chapter 6.5, p. 313), about 479 kJ of

232 energy is stored per mole of CO_2 fixed into photosynthetic products; that is, S_p [W m^{-2}] = −0.479
233 F_{CO_2} [μmol m^{-2} s^{-1}]. For example, a canopy assimilation rate of F_{CO_2} =10 μmol m^{-2} s^{-1} equates to
234 energy flux of S_p = 4.79 ≈ 5 W m^{-2} (cf., Meyers and Hollinger 2004, their Fig. 5 and Masseroni
235 et al. 2014, their Fig. 3). Thus, the photosynthesis storage term is relatively small; according to
236 estimate by Finnigan (2008), $S_p \approx 0.01 R_{net}$. The canopy heat storage term (e.g., because of
237 changes in leaf temperature), S_c, may be also a factor in the lack of closure, but it cannot be
238 easily assessed and flux values cannot be easily corrected for this influence in the framework of
239 our study. According to Meyers and Hollinger (2004, Figs. 4 and 5) and Masseroni et al. (2014,
240 Fig. 3), generally $S_c \leq S_p$. Although the soil heat flux G in Eq. (5) and the storage terms S_a and
241 S_g in Eq. (7) can be estimated from the observations, their contribution to SEB closure at half-
242 hourly time scales lies beyond the scope of this study.
243 The SEB (1) and the fact that the turbulent fluxes are highly correlated with the net
244 radiation (e.g., see plots presented in Sub-section 4.3 shortly) provide an objective approach to
245 estimate turbulent fluxes independently of a conventional bulk flux algorithm. Traditionally, the
246 SEB is considered closed in numerical models of the climate system and in other applications
247 (e.g., for remote sensing), allowing for estimation of missing terms as the residual of the others
248 (e.g., Cuxart et al. 2015 and references therein). Similar ideas are used in soil-vegetation-
249 atmosphere transfer schemes where H_S and H_L are estimated from thermal infra-red data (i.e.
250 radiometric surface temperature) and SEB, Eq. (1) (e.g., Priestley and Taylor 1972; Su 2002;
251 Kustas et al. 2004; Ezzahar et al. 2012; Yao et al. 2015 and references therein).
252
253 **3. Observation Site and Instrumentation**
254

Figure 1 shows the study area located along the Columbia River Gorge in eastern Oregon and Washington states. This region was chosen because of its combination of complex terrain and extensive wind farm development. These measurements provide insight into the structure and evolution of atmospheric flows and other physical processes in complex terrain leading to improvements in parametrization of subgrid-scale processes in NWP models to support wind energy forecasting (see Bianco et al. 2019; Olson et al. 2019; Shaw et al. 2019; Wilczak et al. 2019). Federal agencies, private companies, and universities collaborated on the WFIP 2 project, deploying wind profiling radars, sodars, lidars, networks of tall meteorological towers, and other instruments across a range of spatial scales (Figs. 1 and 2).

In this observational study we use measurements of half-hourly averaged turbulent and radiative fluxes, surface meteorology, and basic soil parameters from the Physics Site 1 tower (PS01, 45.64°N and 120.68°W) located near Wasco, Oregon, (Fig. 1) to examine SEB closure over different soil conditions (dry, wet, and frozen) and at different averaging timescales. Turbulent fluxes and mean meteorological data were measured continuously on a 10-m meteorological tower at two levels, nominally 3 m and 10 m (Fig. 2). Each level was instrumented with identical fast response three-axis sonic anemometers sampling wind velocity and sonic temperature at 20 Hz (R.M. Young Model 81000) and Rotronics HC2S3 temperature and relative humidity probes (T/RH, sampling frequency = 1 Hz). The HC2S3 probes were housed in ventilated radiation shields. A fast-response (20 Hz) open path infrared gas analyzer (LI-7500, LI-COR Inc.) was collocated at 3-m height with the lower sonic anemometer for direct measurements of water vapor turbulent flux and other relevant turbulent statistics. Measurements were collected by a data-logger (Campbell CR3000) and successively parsed into 15-minute data files for cell-modem network transmission to remote data storage.

278 Tower-based eddy covariance measurements provide a long-term near continuous
279 temporal record of half-hourly averaged turbulent momentum, mass, and energy fluxes. The
280 mean wind speed and wind direction were derived from the sonic anemometers, with rotation of
281 the measurement axes to place the measured wind components in a streamline coordinate system
282 based on half-hour averaged 20-Hz data. In this study, we performed tilt-corrections of the sonic
283 anemometer data using the "planar-fit" method rotation of the coordinate system proposed by
284 Wilczak et al. (2001), which essentially fits a climatological plane through the streamlines of the
285 local flow. The planar-fit angles were calculated from 30-min averages at each level over the 10-
286 month dataset (for the period 24 June 2016 to 01 May 2017). Several data-quality indicators
287 based on objective and subjective methods have been applied to the original flux data to remove
288 spurious or low-quality records. Specifically, turbulent data have been edited for unfavorable
289 relative wind direction for which the tower was upwind of the sonic anemometers, non-
290 stationarity, minimum or/and maximum thresholds for the turbulent statistics, etc. (e.g., Bariteau
291 et al. 2010; Grachev et al. 2011; Grachev et al. 2015; Blomquist et al. 2014 and references
292 therein). In particular, sonic anemometer data based on the planar-fit procedure were flagged as
293 bad if mean vertical velocity component differed by more than 0.2 m s^{-1} from the plane.
294 Measurements of soil temperature and moisture were made at five levels located
295 nominally at 5, 10, 20, 50, and 100 cm depths below the ground surface approximately 5 m from
296 the flux tower. Campbell Scientific 107 temperature sensors and a CS616 water content
297 reflectometer were used to measure temperature and soil moisture (in volumetric water content)
298 respectively. No direct measurements of surface soil heat flux with a heat flux plate were
299 performed at this site. The soils at the WFIP 2 Physics Site PS01 are primarily well-drained silt

300 (73%), with minor components of sand (14%), and clay (13%) and average 152 cm in depth
301 before reaching harder rock (water table).
302 The downwelling and upwelling radiation was measured from two radiation masts
303 located near the flux tower (Fig. 2). Eppley pyranometer (PSP) and pyrgeometer (PIR) are used
304 to measure the shortwave and infrared radiation. Both 'slow'-response radiation and soil data
305 reported here are based on raw measurements sampled at 1 Hz which were subsequently
306 averaged over 1-min time intervals and recorded by a data-logger. The instrument suite located
307 on the tower was operated by University of Notre Dame scientists; solar radiation and soil
308 science instruments were conducted by the NOAA/ESRL team.
309
310 **4. Analysis of the WFIP 2 Data**
311
312 *4.1. Time Series*
313
314 In this sub-section, we analyze the time series of half-hour averaged surface fluxes and
315 basic meteorological variables to describe weather and soil conditions, surface fluxes, and other
316 relevant variables as observed during the entire WFIP 2 field campaign for the period 24 June
317 2016 to 01 May 2017 (Year Days 176-487 with respect to January 1, 2016 UTC). Figures 3 and
318 4 show the time series of 'slow' half-hourly averaged basic meteorological variables collected at
319 the Physics Site PS01 near Wasco, Oregon (Fig. 2), except for the rain rate which was measured
320 near another observational site located near the Wasco State Airport (WCO). Figure 5 shows the
321 time series of short-wave (SW) and long-wave (LW) radiation (downwelling and upwelling),
322 radiation budgets, and also the surface albedo observed at Physics Site PS01. By convention,

radiation fluxes are positive when directed toward the surface, fluxes away are negative. The net radiation describes the balance between incoming (downwelling) and outgoing (upwelling) SW and LW radiation. The surface albedo (reflectivity of a surface) in Fig. 5d is derived from the ratio of the upwelling SW radiation (i.e., reflected from the surface) to the downwelling SW radiation. Time series of the half-hour averaged friction velocity $u_* = \sqrt{-\overline{w'u'}}$, sensible H_S and latent H_L heat fluxes defined by Eqs. (3)–(4) are shown in Fig. 6.

Figure 3b shows that the prevailing winds have a bimodal distribution with the two dominant wind directions ~ 180° apart (easterly and westerly winds). These predominant winds generally blow parallel to the ridge in the Fig.2. The air and soil temperatures display the familiar strong seasonal trend with maximum in mid-summer and minimum during winter (Figs. 3c and 4a). The seasonal pattern of the air temperature (Fig. 3c) is highly correlated with soil thaw and freeze (Figs. 4a and 5d). The onset of near-surface soil freezing occurred in the autumn on about days 343–344 (8–9 December 2016). Frozen ground started warming when the gradient of the subsurface temperature changed sign on about days 428–429 (3–4 March 2017). The air temperatures rise above freezing during spring melt on about days 424–425 (27–28 February 2017) and eventually reaches a summer maximum (Fig. 3c). The rather constant temperature of the soil at 5 and 10-cm levels near 0°C (Fig. 4a) on about days 344–428 (9 December 2016–3 March 2017) is due to the snow cover when present (cf. Fig. 5d), to the rather high moisture content of the soil (Fig. 4b), and to releasing latent heat of fusion of soil water as soil freezes. The near-zero topsoil temperatures on these days are due to the phase transition of water to ice and are associated with the so-called "zero-curtain" effect (e.g., Grachev et al. 2018 and reference therein). Release of latent heat during the freezing of pore water results in the maintenance of isothermal temperatures at or around 0°C within the freezing ground layer over

346 extended periods (Fig. 4a). The zero curtain decouples the soil from the atmosphere, preventing
347 cooling in the underlying ground layer (zero soil heat flux) for its duration (e.g., see Grachev et
348 al. 2018 Figs. 9c and 9d) and thus protecting the ground from severe freezing.
349 The date of the first snowfall and the occurrence of the snow-free date are determined
350 radiometrically as the date when the surface albedo first rises above and drops below 30%
351 respectively (Stone et al. 2002). This behaviour of the albedo around a first snowfall/melt date is
352 associated with a distinguishing feature of the upwelling (reflected) SW solar radiation which is
353 changes rapidly during snowfall and snowpack disintegration, i.e., during the transition from the
354 low-albedo bare soil to snow cover and vice versa. According to Fig. 5d, the albedo increases
355 suddenly on days 342–344 (7–9 December 2016) with the first snowfall in the vicinity of the flux
356 tower. The date of snow melt is evidenced by the large reduction in albedo that occurs on days
357 425–426 (28 February–1 March 2017), i.e., when the snow cover essentially disappears (Fig.
358 5d). These dates of the first snowfall and snow melt are in close correspondence with the dates of
359 the soil freezing and melt derived independently from the temperature measurements.
360 The annual cycle of the downwelling SW radiation SW_{down} at half-hourly resolution is
361 clearly evident with maximum flux values in mid-summer of about 940 to 960 W m^{-2} (Fig. 5a)
362 and values that drop to minimum during winter months. Similarly, the downwelling longwave
363 radiation LW_{down} reaches a minimum in winter and a maximum in summer (Fig. 5b). A net
364 longwave radiative loss (difference between blue and red symbols in Fig. 5b) occurs throughout
365 the year (Fig. 5c). Hence, the net radiation R_{net} is weakly negative during winter months (Fig.
366 5c). The peak in R_{net} occurs during spring/summer when the snow melts and the surface albedo
367 reaches the low summertime values and SW_{down} is near the annual peak (Fig. 5).

368 Figure 6 shows the seasonal cycles of the friction velocity and the turbulent fluxes of the
369 sensible heat, and latent heat at half-hourly resolution. It is obvious that friction velocity (Fig. 6a)
370 and the wind speed (Fig. 3a) are highly correlated to one another. The annual course of the
371 sensible heat flux and the net radiation, R_{net} are qualitatively very similar (cf. Figs. 5c and 6b)
372 because the balance between solar and longwave radiation is the principal energy source for
373 daytime surface warming and evaporation (see Eq. (1)). Concurrently, the annual course of the
374 latent heat flux shown in Fig. 6c depends on both R_{net} according to Eq. (1) and soil moisture
375 (Fig. 4a). Figure 6 shows that during the winter and cold seasons, the sensible and latent heat
376 fluxes were small and mostly irregular when the ground is covered with snow and air
377 temperatures are generally below freezing. However, the turbulent fluxes increase rapidly in
378 magnitude when air temperatures rise above freezing during spring melt and eventually reach a
379 summer maximum (cf. Figs. 3 and 6). During late summer and early autumn all turbulent fluxes
380 rapidly decrease in magnitude when the air temperature decreases and falls below freezing.
381 Based on the seasonal behaviour of the surface fluxes and surface meteorology shown in
382 Figs. 3-6 for the entire field campaign (from 24 June 2016 to 01 May 2017), we sort the data into
383 three categories separated by threshold values deduced from the time series of soil temperature
384 (Fig. 4a) and soil moisture at 5 cm depth (Fig. 4b). We distinguish three soil conditions (see also
385 Figs. 4d and 6d):
386 (i) Dry bare or lightly vegetated soil surfaces, the soil temperature at 5 cm depth > 1°C and the
387 soil moisture at 5 cm depth ≤ 0.07;
388 (ii) Wet bare or lightly vegetated soil surfaces, the soil temperature at 5 cm depth > 1°C and the
389 soil moisture at 5 cm depth > 0.07;
390 (iii) Frozen (snow covered) soils surfaces, the soil temperature at 5 cm depth ≤ 1°C.

391 Soil moisture content above is measured as the ratio of the volume of liquid water to soil volume.

392

393 *4.2. SEB at different timescales*

394

395 In this and next sub-sections, we consider, first, the incomplete the energy balance
396 equation, $H_S + H_L$ versus R_{net}; that is, Eq. (1) without the ground heat flux term G since direct
397 measurements of G (by a flux plate) were not available. Further in Sub-section 4.5 we will
398 estimate the soil heat flux G in Eq. (1) based on the available information (soil temperature and
399 moisture, upwelling longwave radiation) to evaluate influence of G for the "complete" SEB
400 closure equation, $H_S + H_L + G$ versus R_{net}, at different temporal scales for the entire dataset and
401 separately for different soil types. Thus, the incomplete SEB closure equation (without the
402 ground heat flux G) is based only on the direct measurements of the surface fluxes H_S, H_L, and
403 R_{net}; whereas, the "complete" SEB closure equation (with G) is based on the direct
404 measurements of H_S, H_L, R_{net} plus modelled G (indirect estimates).

405 The closure of the incomplete SEB during the entire field campaign is shown in Fig. 7.
406 Fig. 7a shows a scatter plot of the sum of the sensible and latent heat fluxes versus the net
407 radiation for half-hourly averaged fluxes. Fig. 7b presents a similar plot based on daily, monthly,
408 and sub-annual (311 days) averages. Note that the daily, weekly, monthly etc. data points in this
409 study are derived from the original half-hourly averaged fluxes averaged over longer time scales.
410 Our direct measurements of SEB in Fig. 7a are roughly consistent with past eddy-covariance
411 results over land showing that the sum of H_S and H_L systematically underestimate the net
412 radiation for $R_{net} > 0$ (generally during daytime convective conditions) and overestimate for
413 $R_{net} < 0$ (generally during nocturnal boundary layer). According to Fig. 7a, the linear regression

forced through the origin for the half-hourly data is $y = 0.77x$ with the correlation coefficient R^2 = 0.94 (number of data points, $N = 3624$) in the case $R_{net} > 0$ (dashed magenta line) and the regression is $y = 0.27x$ with $R^2 = 0.41$ and $N = 897$ in the case $R_{net} < 0$ (dotted red line). In total for both positive and negative R_{net} the linear regression forced through the origin is $y = 0.76x$ (not shown) with $R^2 = 0.95$ and $N = 4521$.

Thus, the SEB imbalance for half-hourly averaged fluxes over the entire WFIP 2 field campaign (from 24 June 2016 to 01 May 2017) is about 24%. This mean imbalance is generally consistent with other efforts to close the SEB (e.g., Foken and Oncley 1995; Wilson et al., 2002; Meyers and Hollinger 2004; Foken et al., 2006; Oncley et al. 2007; Cava et al. 2008; Foken 2008; Jacobs et al. 2008; Panin and Bernhofer 2008; Higgins 2012; Leuning et al., 2012; Stoy et al., 2013; Masseroni et al., 2014; Cuxart et al., 2015; Gao et al., 2017a). Despite multiple review papers that discuss the lack of energy closure at half-hourly and hourly averaged timescales, and the myriad of studies devoted to the investigation of the individual factors of the imbalance at these averaging period, the SEB closure at the longer averaging times (from the daily to sub-annual timescales) has not been systematically examined. In recent years, several papers (e.g., Finnigan et al. 2003; Mauder and Foken, 2006; Leuning et al. 2012; Charuchittipan et al. 2014; Reed et al. 2018) have worked to address this issue, however, there is no consensus on how to improve energy closure.

Foken et al. (2006) applied the ogive analysis to the data measured over a maize field of the LITFASS-2003 experiment and was focused mainly on data from three selected days, where the averaging time was extended up to 4 hours. According to Charuchittipan et al. (2014), extension of the averaging time by a few hours does not significantly improve the energy balance. Previous work by Leuning et al. (2012) has shown that energy closure is observed at

437 only 8% of flux sites in the La Thuile synthesis dataset (produced after a workshop in La Thuile,
438 Italy, in February, 2007) with half-hourly averages but this increases up to 45% of sites using
439 daily averages. Recent work by Reed et al. (2018) examined the effect of temporal variation in
440 the SEB for different site locations and seasons at annual and sub-annual timescales. Here, we
441 focus on the longer averaging time intervals than in the papers mentioned above; that is,
442 substantially longer daily averages (up to annual timescales).

443 Our data shows that, in general, increasing the averaging time consistently from half-
444 hourly to daily and longer time intervals substantially reduces the SEB imbalance. According to
445 Fig. 7b, the linear regression forced through the origin is $y = 0.85x$ with the correlation
446 coefficient $R^2 = 0.93$ ($N = 243$) in the case of daily averages (green circles and dashed magenta
447 line) and in the case monthly (30-day) averages the regression is $y = 0.91x$ with $R^2 = 0.99$ and N
448 = 10 (i.e., ten full months, blue triangles and dotted red line). Moreover, the SEB can be closed
449 for this site within several percent on sub-annual timescale (red star); that is, $< H_S > + < H_L >$
450 $= 1.02 < R_{net} >$ where $< \cdots >$ denotes an averaging operator (the arithmetic mean) for all
451 available half-hourly values of the surface energy fluxes during the entire field campaign (311-
452 day dataset). In this case, $N = 1$ (one data point). Given sufficient data, it would be ideal for these
453 purposes to average half-hourly or hourly data for a full year without large gaps (365-day
454 averaging for a common year).

455 On average, the scatter plots of the daily and monthly averaged data (Fig. 7b) show
456 substantial reduction of the incomplete SEB imbalance as compared with the half-hourly
457 averages. However, imbalances between the turbulent fluxes and the available energy may be
458 worse at daily timescales (cf., Leuning et al., 2012), and in a select number of cases still occur in
459 the monthly averages (cf., Reed et al., 2018), implying some processes extend beyond daily and

460 monthly timescales. In the next sub-section, we consider some of the factors leading to these
461 biases.
462
463 *4.3. SEB over different types of soil surfaces*
464
465 In this sub-section we consider the incomplete SEB and the surface energy fluxes over
466 the entire field campaign at half-hour and longer averaging time scales separately for the three
467 soil conditions identified in Section 4.1. Figure 8 shows scatter plot of the turbulent flux terms in
468 Eq. (1) versus R_{net} at half-hourly resolution observed from 24 June 2016 to 01 May 2017 for
469 three different soil surfaces (dry, wet, and frozen). Recall also that the soil heat flux, G, which
470 was not measured, is not used here for the SEB closure analysis (e.g., in Figs. 7 and 8). The
471 turbulent fluxes of the sensible and latent heat shown in Fig. 8a, b increase systematically with
472 increasing net radiation because R_{net} is normally the principal source of energy for daytime
473 warming of the surface and evaporation. We note different slopes of the bin-averaged fluxes
474 (solid lines) for different soil conditions. According to Fig. 8a, the bin-averaged dependence of
475 H_S is generally steeper for drier than for wetter soils, whereas the situation with H_L is obviously
476 opposite; the latent heat flux is small over dry soil surfaces indicating that evaporation is
477 negligible (Fig. 8b). Note also that sensible and latent heat fluxes are comparable over wet soil
478 surfaces (cf. Figs. 8a and 8b) and the Bowen ratio $Bo = H_S/H_L$ averaged around 1 during
479 daytime (not shown). The different behavior of the turbulent fluxes in Fig. 8 for different soil
480 conditions is perhaps due to the different physical properties of the soils. It can be assumed that
481 wet and/or water-saturated soils, which have larger heat storage due to high specific heat
482 capacity and higher thermal conductivity, cause the observed behaviour of H_S and H_L versus

483 R_{net} (Fig. 8a and 8b). If the soil surface is frozen, both H_S and H_L are small and highly variable
484 as mentioned earlier (cf. Fig.6).

485 According to the bin-averaged data in Fig. 8c, the sum $H_S + H_L$ is further from closure
486 for wet soils compared to dry soils. The statistical dependence of the turbulent fluxes and R_{net}
487 for frozen soil surfaces appears weak, if not non-existent (Fig. 8c). As mentioned in Section 4.1,
488 during the cold season topsoil temperatures remain close to 0°C and the soil heat flux term in Eq.
489 (1) $G = 0$ for an extended period of time. This isothermal freezing process is referred to as the
490 "zero-curtain" effect (e.g., Grachev et al. 2018). Under such conditions, the latent heat of fusion
491 term must be added to Eq. (1). The nature of this term is associated with the change between the
492 liquid and solid phases, as when water turns to ice. The absence of the latent heat of fusion term
493 in the SEB equation explains why Eq. (1) doesn't work for the case of frozen soil surfaces as
494 shown in Fig. 8c. However, a detailed discussion of the SEB during the zero-curtain period is
495 beyond the scope of this paper.

496 The linear regression forced through the origin (not shown) for the dry soil data shown in
497 Fig. 8c is $y = 0.79x$; that is, the SEB imbalance is 21% in this case. For wet soils over the entire
498 field campaign (Fig. 8c), the linear regression forced through the origin is $y = 0.72x$, implying
499 that there is an imbalance of 28%, which is high but not unusual. The linear regression of Fig. 8c
500 for the frozen (snow covered) soil surfaces is $y = 0.096x$, implying a weak correlation between
501 the turbulent fluxes and the net radiation. Thus, the surface energy balance in the form of Eq. (1)
502 cannot be applied to freezing soil surfaces without the inclusion of a latent heat of fusion term.

503 Our results for the SEB closure over dry and wet soils are consistent with prior studies.
504 According to Roxy et al. (2014), SEB closures were lower when the latent heat fluxes were
505 highest, mainly during wet periods; the mean SEB closure was found to be 0.742 and 0.795 for

506 wet and dry seasons, respectively. Cuxart et al. (2015) reported that very large imbalances are
507 related to high values of soil moisture, especially in warm conditions. However, a multi-year
508 analysis of the surface energy balance in a semi-arid savanna ecosystem in South Africa by
509 Majozi et al. (2017) revealed a SEB closure of 0.93±0.11 with the dry season having the highest
510 energy imbalance (0.70) while the mean SEB closure during the wet season was 1.12.
511 Figure 9 shows that increasing the averaging time from half-hourly to daily and longer
512 time intervals substantially reduces the SEB imbalance for each soil type (though with some
513 reservations for the frozen soils). For dry soils in Fig. 9a, the linear regression for daily averages
514 forced through the origin is $y = 0.92x$ and the SEB can be closed within one percent on a
515 seasonal timescale (red six-pointed star). For wet soils (Fig. 9b), the linear regression of daily
516 averages is $y = 0.79x$ and the SEB closure is ≈ 0.95 at a seasonal timescale. For frozen soil
517 surfaces (Fig. 9c), the SEB closure is ≈ 0.06 at daily timescales and ≈ 0.34 at a seasonal
518 timescale.
519 Although, increasing the averaging time from half-hourly (Fig. 8c) to daily and longer
520 time intervals (Fig. 9) consistently reduces the SEB imbalance in general for each specific soil
521 condition, the situation is not so obvious if we compare the SEB imbalance between different
522 soil types. For example, the SEB closure at half-hourly resolution for dry soils (≈ 0.79) may be
523 approximately the same as the SEB closure for wet soils (≈ 0.79) at longer (daily) timescales. In
524 addition, the SEB imbalance may be worse at monthly timescales for wet (≈ 0.86) and frozen (≈
525 0.19) soils compared to daily averages (≈ 0.92) for dry soils. Thus, our results support and clarify
526 previous findings by Leuning et al. (2012) and Reed et al. (2018) where in a select number of
527 cases, increasing the averaging time does not always lead to reduction of the SEB imbalance
528 because SEB closures were compared for different sites or different seasons.

529

530 *4.4. Case studies: the uninterrupted time series ("golden files")*

531

532 In the previous sections, we considered the incomplete SEB imbalance based on
533 measurements over the entire WFIP 2 field campaign (311-day dataset from 24 June 2016 to 01
534 May 2017) with and without separation into the three different soil conditions identified in
535 Section 4.1. However, the original in situ data often contain gaps, from very short (half-hour to
536 few hours) up to relatively long (few weeks, Figs. 3-7). Occasional gaps in the data time series
537 are mainly due to equipment failures, calibrations and maintenance operations or general system
538 breakdown. Data quality assurance/control procedures lead to the rejection of "bad" data,
539 generating additional gaps in the data records. For example, turbulent data were edited for
540 spikes, unfavorable relative wind directions, non-stationarity, etc. Averaging of the fragmented
541 data sets raises issues in the interpretation of the results. Gap-filling techniques are commonly
542 used to estimate the missing data; for example, short gaps in data can be filled by interpolation.
543 However, a gap-filling procedure replaces missing empirical data by simulated synthetic values
544 that can introduce more errors.

545 To overcome these limitations, we consider the longest available uninterrupted time
546 series of relatively good data for each soil condition defined in Section 4.1 ("golden files").
547 Figures 10-12 show continuous monthly (30-day long) records of the SEB components for dry,
548 wet, and frozen soils respectively. From data in Figs. 10-12, the mean incomplete SEB closure
549 (the slope of a linear regression line with forced origin) for half-hourly averaged data is ≈ 0.80
550 for the dry soils (N = 1405), ≈ 0.73 for wet soils (N = 1201), and ≈ 0.12 for frozen soils (N =
551 988). Note that the number of the half-hourly averaged data points in the case of dry (Fig. 10),

552 wet (Fig. 11), and frozen (Fig. 12) soils is less than the maximum amount possible for one month
553 (N = 1440 = 48×30) due to quality control. For daily averages the mean incomplete SEB closure
554 is ≈ 1.02, ≈ 0.82, and ≈ 0.22 for dry (Fig. 10), wet (Fig. 11), and frozen (Fig. 12) soils
555 respectively (N = 30 for each soil type). Thus, the incomplete SEB can be closed for the dry soil
556 within about two percent on a daily timescale for "golden files" data in Fig. 10. Further, the mean
557 incomplete SEB closure based on the one-month averages for the data in Figs. 10-12 are ≈ 1.06
558 (dry soil), ≈ 0.86 (wet soil), and ≈ 0.19 (frozen soil). Thus, the results based on the almost
559 uninterrupted 30-day time series of fluxes ("golden files", Figs. 10-12) support our previous
560 findings derived from the data collected during the entire 311-day field campaign (gapped time
561 series). That is: (i) increasing the averaging time from half-hourly to daily and monthly intervals
562 generally reduces the incomplete SEB imbalance for specific type of soil; and (ii) the incomplete
563 SEB closure is lower for the wet soils compared to dry soils (e.g., 0.73 vs. 0.80 respectively at
564 half-hourly resolution), while closure is only ≈ 12% for frozen soils, apparently due to the lack of
565 a latent heat of fusion term in (1). One can estimate the missing latent heat of fusion term in (1)
566 should be ≈ 0.8-0.9 of R_{net} to close the SEB during the cold season.

567 As expected, the SEB flux components and the topsoil temperature difference series have
568 a pronounced diurnal cycle (rising and falling patterns) for both dry and wet soils (Figs. 10 and
569 11), whereas for frozen soils (Fig. 12) such a cycle is much less evident (with some exceptions of
570 the net radiation, Fig. 12a). On the diurnal time scale, variations in the turbulent heat fluxes are
571 dominantly forced by daily rhythms in the incoming solar radiation, which also drives changes in
572 the air and soil temperatures. Furthermore, diurnal variations of the residual energy are also
573 observed for both dry (Fig. 10c) and wet (Fig. 11c) soils. According to Figs. 10c and 11c, the
574 daily patterns of the residual energy are characterised by positive values during the first part of

575 the day and by a sign reversal in the second half of the day. Thus, the observed daily patterns of
576 the residual energy (Figs. 10c and 11c) confirm that the SEB is more easily balanced at daily
577 averaging timescales than half-hourly because of the cancellation of energy residuals of opposite
578 sign. The diurnal variations of the residual energy reported here (Figs. 10c and 11c) are generally
579 in good agreement with previously published results (e.g., Lamaud et al. 2001; Cava et al. 2008;
580 Higgins 2012). The difference of the soil temperature between 10 cm and 5 cm levels for dry,
581 wet, and frozen soils is shown in Figs. 10d, 11d, and 12d respectively. This temperature
582 difference is ultimately related to the ground heat flux G through Eq. (8). In general, the diurnal
583 cycle of solar radiation modulates a sinusoidal variation of the temperature difference in top soil
584 layer (Figs. 10d and 11d) and, therefore, the ground surface heat flux and diurnal temperature
585 waves. Thereby, much of the energy that enters the soil during the day returns to the atmosphere
586 at night through terrestrial longwave radiation. For this reason, G is often the smallest component
587 of the daily surface energy balance (solid blue lines in Figs. 10d and 11d). The near-zero
588 temperature difference in the top soil layer during the freezing period (Fig. 12d) is associated
589 with near isothermal temperatures at or around 0°C (zero soil heat flux) and the "zero-curtain"
590 effect as discussed in Sub-section 4.1 earlier.
591 Figure 13 summarizes the incomplete SEB closure equation (without the ground heat flux
592 G) at different temporal scales discussed in Sub-sections 4.2-4.4. The red symbols and lines in
593 Fig. 13 represent all measurements. The SEB imbalance categorized by soil condition are shown
594 in Fig. 13 as green symbols and green dash line (dry soils), blue symbols and blue dash line (wet
595 soils), and cyan symbols and cyan dash line (frozen soils), respectively. The averaged SEB
596 values plotted on this graph for three different soil types are derived from the entire 311-day field
597 campaign except the monthly averages that are based on the uninterrupted 30-day time series for

598 each type of soil shown in Figs. 10-12 ("golden files"). Averaging operator $< \cdots >$ in Fig. 13
599 denotes the arithmetic mean of the all available original 30-min surface energy fluxes through
600 temporal averaging for a specific timescale (daily, weekly, monthly, seasonal and sub-annual).
601 Figure 13 is the visual representation of our primary findings; that is, increasing the averaging
602 time consistently from half-hourly to longer time intervals substantially reduces the SEB
603 imbalance and the closure is lower for the wet soils as compared to dry soils whereas the SEB
604 closure for frozen soils is very poor, if not non-existent.
605
606 *4.5. Soil heat flux evaluation at different temporal scales*
607
608 The purpose of this study is not to investigate closure of the SEB at standard half-hourly
609 time scales (or forcing SEB closure based on the direct measurements of all SEB components
610 mentioned in Section 2). Instead, in this study we evaluate SEB closure over a range of
611 timescales from half-hourly to daily, monthly, seasonal and even sub-annual averaged timescales
612 based on the available direct measured fluxes H_S, H_L, and R_{net}. In other words, we consider the
613 SEB closure at long time intervals (up to annual timescales) through temporal averaging of the
614 original 30-min data. These time intervals are substantially longer daily averages than those
615 considered in many previous studies (see Section 4.2). In this section we consider estimates of
616 the soil heat flux G in (1) and its impact on the SEB closure at different temporal scales.
617 As mentioned earlier, we do not have direct measurements of the soil heat flux during the
618 WFIP 2 field campaign. Moreover, directly measuring G is a challenging problem in general.
619 Thus, there are numerous approaches to compute the soil heat flux, that use different input data
620 from in situ measurements (e.g., see Liebethal et al. 2005; Liebethal and Foken 2007; Gao et al.

621 2017b; Yang and Wang 2008 and references therein). Different methods for evaluating G can use
622 various in situ measurements such as soil temperature, soil moisture, net radiation, etc. In
623 addition, some parameterization approaches can be suitable for different times of the day. The
624 most common approach for determining G is the calorimetric method (e.g., Liebethal et al.
625 2005). Some other approaches proposed G as a simple fraction (linear or nonlinear function) of
626 the net radiation (e.g., Gao et al. 2017b and references therein). Liebethal and Foken (2007)
627 reviewed six different parameterization approaches for G and compared those with the
628 calorimetric method. In a later study, Gao et al. (2017b) evaluated nine different methods for
629 calculating the soil heat flux at the surface ($z = 0$) by comparing the calculated and measured
630 soil heat flux at 5 cm depth. In this section, we use a traditional calorimetric approach for
631 determining G at the interface (e.g., Liebethal and Foken 2007, Section 3.1; Gao et al. 2017b,
632 Section 2.1), which combines the flux measurements (by a flux plate) or estimations (from Eq.
633 (8)) at some reference depth Δz below the surface and the calorimetry (estimation of the change
634 in heat storage in the layer between the surface and the depth Δz). Recall that in the current
635 study, we consider the SEB closure at time intervals substantially longer than daily averages, and
636 the soil heat flux is relatively small and, therefore, less important as compared with the turbulent
637 and radiative surface fluxes at these scales. However, we estimated G based on the available
638 information to evaluate the influence of G at different temporal scales.
639 Here, we use measurements of soil temperature and moisture to estimate G in (1) based
640 on the Fourier's Law of Heat Conduction (8). We can integrate (8) from the interface down to
641 depth Δz, and relate the flux to the difference in the temperature at the interface to the
642 temperature at depth Δz. Near the surface we can linearly approximate $T(z)$, so according to the
643 calorimetric method

$$G = \frac{\lambda}{\Delta z}[\theta_0 - T_S(\Delta z)] + \frac{1}{2}\rho_S c_{pS}\frac{\partial T_S}{\partial t}\Delta z \quad (9)$$

where ρ_S is the soil density and c_{pS} is the soil specific heat, T_S is the soil moisture measured at 5 cm depth; that is Δz = 5 cm, and $\theta_0 = T_S(0)$ is the surface (skin) temperature estimated from the upwelling (outgoing) longwave radiation, LW_{up}, measurements. Subscripts 'zero' and 'S' in (9) denote surface (a value at the interface $z = 0$) and soil reference height values respectively. Based on our data for the entire experimental period, we estimated the thermal conductivity of the soil λ [W m^{-1} K^{-1}] via

$$\lambda = 0.180 + 1.09Q_{S5} \quad (10)$$

where Q_{S5} [vol/vol] is the soil moisture measured at 5 cm depth. Our estimation (10) is consistent with the coefficients for bare soil from Yao et al (2015) model. We have chosen type 'GRA' (Yao et al. 2015, their Table 1), which includes grassland and barren or sparsely vegetated soil (soil at the PS01 tower site is essentially a plowed fallow field with little vegetation). Note that due to the different the thermal conductivity and heat capacity of the soil, the soil heat flux G of wet soil is significant larger than of dry soil (see Eqs. (9) and (10)).

The results of the SEB closure computations without and with the soil heat flux G in Eq. (1) at different temporal scales for the entire dataset and separately for dry and wet soils are summarized in Table 1. The SEB closure without G (ratio of $H_S + H_L$ to R_{net}) is based only on the direct measurements of the surface fluxes and the data presented in Table 1 correspond to values plotted in Fig. 13; that is, the red symbols for entire dataset, the green symbols for dry soils, and the blue symbols for wet soils, respectively. The SEB closure with G (ratio of $H_S + H_L + G$ to R_{net} in Table 1) is based on the direct measurements of H_S, H_L, R_{net} and G modelled by Eq. (9). The case of frozen soil surfaces was not included in Table 1 because the freezing period is associated with zero soil heat flux, $G = 0$, (the "zero-curtain" effect as discussed in

667 Sub-section 4.1 earlier) and, thus, there is no difference in the SEB closure with and without the
668 soil heat flux G. As expected, taking the soil heat flux into account in the SEB equation
669 substantially reduces the SEB imbalance at the half-hourly time scales. However, the importance
670 of this correction decreases with increasing averaging time from half-hourly to longer intervals
671 (i.e., to daily, monthly, and sub-annual timescales), because energy locally entering the soil in
672 the morning is released in the afternoon and evening; that is, because of the cancellation of the
673 soil heat flux (and other storage terms) of opposite sign. Table 1 also shows that, at all averaging
674 timescales, the SEB closure with G (as well as without G) is lower for wet soils compared to dry
675 soils.
676
677 **5. Concluding Remarks: Summary and Discussion**
678
679 In this study, we present an analysis of the surface energy budget (SEB) based on field
680 observations from the Columbia River Gorge in areas of complex terrain near Wasco, Oregon,
681 during a 10-month long portion of the WFIP 2 field campaign (e.g., Bianco et al. 2019; Olson et
682 al. 2019; Shaw et al. 2019; Wilczak et al. 2019). Measurements of half-hourly averaged turbulent
683 and radiative fluxes, surface meteorology, and basic soil parameters made at the PS01 site (Figs.
684 1 and 2) are used to examine the SEB closure (1) for the entire dataset and separately for
685 different soil conditions (dry, wet, and frozen) at various timescales (from half-hourly to sub-
686 annual averages). Note that similar analysis of energy closure variation over different temporal
687 scales in the literature is rare.
688 We considered (i) the incomplete the energy balance equation, $H_S + H_L$ versus R_{net}; i.e.,
689 Eq. (1) without the ground heat flux term G since direct measurements of G were not available

690 (Sub-sections 4.2 and 4.3), and the "complete" SEB closure equation, $H_S + H_L + G$ versus R_{net}
691 (Sub-sections 4.5). The incomplete SEB closure equation (without the ground heat flux G) is
692 based only on the direct measurements of the surface fluxes H_S, H_L, and R_{net}; whereas, the
693 "complete" SEB closure equation (with G) is based on the direct measurements of H_S, H_L, R_{net}
694 plus modelled G (indirect estimates based on Eq. (9)). We estimated the soil heat flux G in Eq.
695 (1) based on the available information (soil temperature and moisture, upwelling longwave
696 radiation) to evaluate influence of G at different temporal scales for the entire dataset and
697 separately for dry and wet soils (Sub-section 4.5 and Table 1). Including the estimates of the soil
698 heat flux G in the SEB closure equation substantially reduces the SEB imbalance, $H_S + H_L + G$
699 versus R_{net}, for each specific soil condition as compared to the incomplete the energy balance
700 equation, $H_S + H_L$ versus R_{net} especially at half-hourly averaged timescales (Table 1). However,
701 the importance of the soil heat flux decreases at the longer averaging times (from the daily to
702 sub-annual timescales). In addition, to support our findings derived from the gapped time series
703 collected during the entire 311-day field campaign (Sub-sections 4.2 and 4.3), we use the longest
704 available uninterrupted (almost without gaps) 30-day time series of relatively good data ("golden
705 files") for each type of soils (Sub-section 4.4) to overcome limitations associated with the gapped
706 series.

707 Our estimates of the complete and incomplete SEB closure equation are generally
708 consistent with past eddy-covariance results over land showing that at half-hourly resolution the
709 sum of turbulent fluxes of sensible and latent heat typically under balance the positive net
710 radiation by about 20-30% during daytime and overestimate negative net radiation at night (Fig.
711 7a). We note that the SEB-imbalance is a longstanding issue in micro-meteorology. However,
712 increasing the averaging time from half-hourly to longer intervals (i.e., to daily, monthly, and

713 sub-annual timescales) substantially reduces the SEB imbalance (Fig. 7b) and, additionally, the
714 longer averaging times can reduce the influence of instrumental measurement errors (e.g.
715 improper calibration) and sampling uncertainties. We find the SEB can be closed for this site
716 within reasonable limits on seasonal and sub-annual timescales (311-day averaging for the entire
717 field campaign dataset).

718 At all averaging timescales, the SEB closure was lower for wet soils compared to dry
719 soils while closure for frozen soils appears weak, if not non-existent (Fig. 13), likely due to the
720 lack of a latent heat of fusion term in the SEB equation (1). However, the latent heat of fusion
721 term is not significant at annual (or sub-annual) timescales because, on average, heat absorbed
722 from the atmosphere during the spring thaw is subsequently released during the fall freeze. This
723 is a temporal redistribution of energy in the top soil layer due to the water/ice-phase transition of
724 the annual freeze–thaw cycle. The SEB can be closed for dry soil within about two percent on a
725 seasonal timescale (81-day) over the entire dataset (Fig. 9a, Fig. 13, and Table 1) and even on a
726 daily timescale for month-long uninterrupted data records ("golden files", Fig. 10).

727 As mentioned earlier, the purpose of this study is not closure of the SEB at half-hourly
728 time scales, but rather, to evaluate SEB closure over a range of timescales. The problem of
729 surface energy imbalance and the individual factors (e.g., storage terms) that lead to the
730 imbalance at half-hourly and hourly time scales has been widely investigated in many studies
731 (e.g., references in Section 2). Here, we analyze and discuss the balance between net radiation
732 and turbulent sensible and latent heat fluxes. Direct measurements of the soil heat flux (by a flux
733 plate) were not available, which may be seen as a disadvantage, but in many numerical climate
734 models only the net radiation and sensible/latent heat fluxes are used to determine the surface
735 temperature. Thus, SEB closure for these fluxes (Fig. 13) is important. Nevertheless, complete

736 closure is possible at half-hourly and hourly averaged time scales by accurate determination of
737 all SEB components (turbulent, radiative, ground heat fluxes and storage energy terms) and
738 careful attention to all sources of measurement and data processing errors (e.g., Lamaud et al.
739 2001; Jacobs et al. 2008; Leuning et al. 2012).
740
741
742 **Acknowledgements**
743 This work was supported by the National Oceanic and Atmospheric Administration (NOAA)
744 Atmospheric Science for Renewable Energy (ASRE) program and by the U.S. Department of
745 Energy (DoE) DE-EE0007605 interagency agreement that supports DoE FOA DE-FOA-
746 0000984. The University of Notre Dame team was supported by DOE-WFIFP2-SUB-001. HJSF
747 was also supported by NSF grants AGS-1565535 and 1921554. Special thanks go to Prof. Dr.
748 Thomas Foken for the thorough review, critical and helpful comments on improving the
749 manuscript. We also appreciate the constructive comments and suggestions from Dr. Ola
750 Persson.
751
752

753 **References**

754

755 Arya P.S., 1988. *Introduction to Micrometeorology*, Academic Press, San Diego, 307 pp

756 Bariteau L., Helmig D., Fairall C.W., Hare J.E., Hueber J., Lang E.K., 2010. Determination of
757 oceanic ozone deposition by ship-borne eddy covariance flux measurements. *Atmos. Meas.*
758 *Tech*. **3**(2): 441–455. https://doi.org/10.5194/amt-3-441-2010

759 Bianco L., Djalalova I.V., Wilczak J.M., Olson J.B., Kenyon J.S., Choukulkar A., Berg L.,
760 Fernando H.J.S., Grimit E.P., Krishnamurthy R., Lundquist J.K., Muradyan P., Pekour M.,
761 Pichugina Y., Stoelinga M.T., Turner D.D., 2019. Impact of model improvements on 80-m
762 wind speeds during the second Wind Forecast Improvement Project (WFIP2). *Geosci. Model*
763 *Dev. Discuss*. https://doi.org/10.5194/gmd-2019-80

764 Blomquist B.W., Huebert B.J., Fairall C.W., Bariteau L., Edson J.B., Hare J.E., McGillis W.R.,
765 2014. Advances in air-sea CO_2 flux measurement by eddy correlation. *Boundary-Layer*
766 *Meteorol*. **152**(3): 245–276. https://doi.org/10.1007/s10546-014-9926-2

767 Cava D., Contini D., Donateo A., Martano P., 2008. Analysis of short-term closure of the surface
768 energy balance above short vegetation. *Agric. Forest Meteorol*. **148**(1): 82–93.
769 https://doi.org/10.1016/j.agrformet.2007.09.003

770 Charuchittipan D., Babel W., Mauder M., Leps J.-P., Foken T., 2014. Extension of the averaging
771 time of the eddy-covariance measurement and its effect on the energy balance closure
772 *Boundary-Layer Meteorol*. **152**(3): 303–327. https://doi.org/10.1007/s10546-014-9922-6

773 Cuxart J., Conangla L., Jiménez M.A., 2015. Evaluation of the surface energy budget equation
774 with experimental data and the ECMWF model in the Ebro Valley. *J. Geophys. Res. Atmos*.
775 **120**(D3): 1008–1022. https://doi.org/10.1002/2014JD022296.

776 Ezzahar J., Er-Raki S., Marah H., Khabba S., Amenzou N., Chehbouni G., 2012. Coupling soil-
777 vegetation-atmosphere-transfer model with energy balance model for estimating energy and
778 water vapor fluxes over an olive grove in a semi-arid region. *Global Meteorol.* **1**(1): e1.
779 https://doi.org/10.4081/gm.2012.e1
780 Finnigan J., 2008. An introduction to flux measurements in difficult conditions. *Ecological*
781 *Applications*, **18**(6): 1340–1350. https://doi.org/10.1890/07-2105.1
782 Finnigan J.J., Clement R., Malhi Y., Leuning R. Cleugh H.A., 2003. A re-evaluation of long-
783 term flux measurement techniques, Part I: Averaging and coordinate rotation. *Boundary-*
784 *Layer Meteorol.* **107**(1): 1–48. https://doi.org/10.1023/A:1021554900225
785 Foken T., Oncley S.P., 1995. Results of the workshop "Instrumental and methodical problems of
786 land surface flux measurements". *Bull. Am. Meteorol. Soc.* **76**(7): 1191–1193
787 Foken T., Wimmer F., Mauder M., Thomas C., Liebethal C., 2006. Some aspects of the energy
788 balance closure problem. *Atmos. Chem. Phys.* **6**(12): 4395–4402. https://doi.org/10.5194/acp-
789 6-4395-2006
790 Foken T., 2008. The energy balance closure problem: An overview. *Ecological Applications*,
791 **18**(6): 1351–1367. https://doi.org/10.1890/06-0922.1
792 Gao Z., Horton R., Liu H.P., 2010. Impact of wave phase difference between soil surface heat
793 flux and soil surface temperature on soil surface energy balance closure. *J. Geophys. Res.*
794 **115**(D16): D16112. https://doi.org/10.1029/2009JD013278
795 Gao Z., Liu H., Katul G.G., Foken T., 2017a. Non-closure of the surface energy balance
796 explained by phase difference between vertical velocity and scalars of large atmospheric
797 eddies. *Environ. Res. Lett.* **12**(3): 034025. https://doi.org/10.1088/1748-9326/aa625b

798 Gao Z., Russell E.S., Missik J.E.C., Huang M., Chen X., Strickland C.E., Clayton R., Arntzen E.,
799 Ma Y., Liu H., 2017b. A novel approach to evaluate soil heat flux calculation: An analytical
800 review of nine methods. *J. Geophys. Res*. **122**(D3): 6934–6949.
801 https://doi.org/10.1002/2017JD027160
802 Garratt J.R., 1992. *The Atmospheric Boundary Layer.* Cambridge University Press, U.K. 316 pp
803 Grachev A.A., Fairall C.W., Persson P.O.G., Andreas E.L, Guest P.S., 2005. Stable boundary-
804 layer scaling regimes: the SHEBA data. *Boundary-Layer Meteorol.* **116**(2): 201–235. DOI
805 10.1007/s10546-004-2729-0
806 Grachev A.A., Bariteau L., Fairall C.W., Hare J.E., Helmig D., Hueber J., Lang E.K., 2011.
807 Turbulent fluxes and transfer of trace gases from ship-based measurements during TexAQS
808 2006. *J. Geophys. Res.* **116**: D13110. https://doi.org/10.1029/2010JD015502
809 Grachev A.A., Andreas E.L, Fairall C.W., Guest P.S., Persson P.O.G., 2015. Similarity theory
810 based on the Dougherty-Ozmidov length scale. *Quart. J. Roy. Meteorol. Soc.* **141**(690A):
811 1845–1856. https://doi.org/10.1002/qj.2488
812 Grachev A.A., Persson P.O.G., Uttal T., Akish E.A., Cox C.J., Morris S.M., Fairall C.W., Stone
813 R.S., Lesins G., Makshtas A.P., Repina I.A., 2018. Seasonal and latitudinal variations of
814 surface fluxes at two Arctic terrestrial sites. *Climate Dynamics*. **51**(5-6): 1793–1818.
815 https://doi.org/10.1007/s00382-017-3983-4
816 Higgins C.W., 2012. A-posteriori analysis of surface energy budget closure to determine missed
817 energy pathways. *Geophys. Res. Lett*. **39**(19): L19403.
818 https://doi.org/10.1029/2012GL052918

819 Jacobs A.F.G., Heusinkveld B.G., Holtslag A.A.M., 2008. Towards closing the surface energy
820 budget of a mid-latitude grassland. *Boundary-Layer Meteorol*. **126**(1): 125–136.
821 https://doi.org/10.1007/s10546-007-9209-2
822 Kustas W.P.,Daughtry C.S.T., 1990. Estimation of the soil heat flux/net radiation ratio from
823 spectral data. *Agric. Forest Meteorol*. **49**(3): 205–223. https://doi.org/10.1016/0168-
824 1923(90)90033-3
825 Kustas W.P., Daughtry C.S.T., Van Oevelen P.J., 1993. Analytical treatment of the relationship
826 between soil heat flux/net radiation ratio and vegetation indices. *Remote Sens. Environ*.
827 **46**(3): 319–330. https://doi.org/10.1016/0034-4257(93)90052-Y
828 Kustas W.P., Norman J.M., Schmugge T.J., Anderson M.C., 2004. Mapping surface energy
829 fluxes with radiometric temperature. In: D.A. Quattrochi, J.C. Luvall (eds.) *Thermal remote*
830 *sensing in land surface processes*. Boca Raton, Florida: CRC Press, 2004, p. 205–253.
831 Lamaud E., Ogée J., Brunet Y., Berbigier P., 2001. Validation of eddy flux measurements above
832 the understorey of a pine forest. *Agric. Forest Meteorol*. **106**(3): 187–203.
833 https://doi.org/10.1016/S0168-1923(00)00215-X
834 Lettau H., Davidson B., 1957. Exploring the atmosphere's first mile. Vol. I. *Instrumentation and*
835 *data evaluation*. Pergamon Press, New York.
836 Liebethal C., Foken T., 2007. Evaluation of six parameterization approaches for the ground heat
837 flux. *Theor. Appl. Climatol*. **88**(1-2): 43–56. https://doi.org/10.1007/s00704-005-0234-0
838 Liebethal C., Huwe B., Foken T., 2005. Sensitivity analysis for two ground heat flux calculation
839 approaches. *Agric. For. Meteorol*. **132**(3-4): 253–262.
840 https://doi.org/10.1016/j.agrformet.2005.08.001

841 Leuning R., van Gorsel E., Massman W.J., Isaac P.R., 2012. Reflections on the surface energy
842 imbalance problem. *Agric. Forest Meteorol*. **156**: 65–74.
843 https://doi.org/10.1016/j.agrformet.2011.12.002
844 Long I.F., Monteith J.L., Penman H.L., Szeicz G., 1964. The plant and its environment.
845 *Meteorol. Rundsch*. **17**: 97–101
846 Majozi N.P., Mannaerts C.M., Ramoelo A., Mathieu R., Nickless A., Verhoef W., 2017.
847 Analysing surface energy balance closure and partitioning over a semi-arid savanna
848 FLUXNET site in Skukuza, Kruger National Park, South Africa. *Hydrol. Earth Syst. Sci*.
849 **21**(7): 3401–3415. https://doi.org/10.5194/hess-21-3401-2017
850 Mauder M., Foken T., 2006. Impact of post-field data processing on eddy covariance flux
851 estimates and energy balance closure. *Meteorologische Zeitschrift*. **15**(6): 597–609.
852 https://doi.org/10.1127/0941-2948/2006/0167
853 Mauder M., Oncley S.P., Vogt R., Weidinger T., Ribeiro L., Bernhofer C., Foken T., Kohsiek
854 W., De Bruin H.A.R., Liu H., 2007. The Energy Balance Experiment EBEX-2000. Part II:
855 Intercomparison of eddy-covariance sensors and post-field data processing methods.
856 *Boundary Layer Meteorol*. **123**(1): 29–54. https://doi.org/10.1007/s10546-006-9139-4
857 Masseroni D., Corbari C., Mancini M., 2014. Limitations and improvements of the energy
858 balance closure with reference to experimental data measured over a maize field. *Atmósfera*,
859 **27**(4): 335–352. https://doi.org/10.1016/S0187-6236(14)70033-5
860 Meyers T.P., Hollinger S.E., 2004. An assessment of storage terms in the surface energy balance
861 of maize and soybean. *Agric. Forest Meteorol*. **125**(1-2): 105–115.
862 https://doi.org/10.1016/j.agrformet.2004.03.001

Nobel P.S., 2009. *Physicochemical and Environmental Plant Physiology*. Fourth Edition, Elsevier Academic Press, Oxford UK, 582p.

Olson J.B., Kenyon J.S., Djalalova I., Bianco L., Turner D.D., Pichugina Y., Chokulkar A., Toy M.D., Brown J.M., Angevine W., Akish E., Bao J.-W., Jimenez P., Kosović B., Lundquist K.A., Draxl C., Lundquist J.K., McCaa J., McCaffrey K., Lantz K., Long C., Wilczak J., Banta R., Marquis M., Redfern S., Berg L.K., Shaw W., Cline J., 2019. Improving wind energy forecasting through numerical weather prediction model development. *Bull. Amer. Meteorol. Society*. https://doi.org/10.1175/BAMS-D-18-0040.1

Oncley S.P., Foken T., Vogt R., Kohsiek W., DeBruin H.A.R., Bernhofer C., Christen A., van Gorsel E., Grantz D., Feigenwinter C., Lehner I., Liebethal C., Liu H., Mauder M., Pitacco A., Ribeiro L., Weidinger T. (2007) The energy balance experiment EBEX-2000, Part I: Overview and energy balance. *Boundary Layer Meteorol*. **123**(1): 1–28. https://doi.org/10.1007/s10546-007-9161-1

Panin G.N., Bernhofer C., 2008. Parametrization of turbulent fluxes over inhomogeneous landscapes. *Izvestiya, Atmos. Ocean. Phys*. **44**(6): 701–716. https://doi.org/10.1134/S0001433808060030

Priestley C. and Taylor R., 1972. On the assessment of surface heat flux and evaporation using large-scale parameters. *Mon. Wea. Rev*. **100**(2): 81–92.

Reed D.E., Frank J.M., Ewers B.E., Desai A.R., 2018. Time dependency of eddy covariance site energy balance. *Agric. Forest Meteorol*. **249**: 467–478. https://doi.org/10.1016/j.agrformet.2017.08.008

884 Roxy M.S., Sumithranand V.B., Renuka, G., 2014. Soil heat flux and day time surface energy
885 balance closure at astronomical observatory, Thiruvananthapuram, south Kerala. *J. Earth*
886 *Syst. Sci*. **123**(4): 741–750. https://doi.org/10.1007/s12040-014-0437-9
887 Sauer T.J., Hatfield J.L., Prueger J.H., Norman J.M., 1998. Surface energy balance of a corn
888 residue-covered field. *Agric. Forest Meteorol*. **89**(3–4): 155–168.
889 https://doi.org/10.1016/S0168-1923(97)00090-7
890 Shaw W., Berg L., Cline J., Draxl C., Djalalova I., Grimit E., Lundquist J.K., Marquis M.,
891 McCaa J., Olson J., Sivaraman C., Sharp J., Wilczak J.M., 2019. The second Wind Forecast
892 Improvement Project (WFIP2): General overview. *Bull. Amer. Meteorol. Society*. **100**(9):
893 1687–1699. https://doi.org/10.1175/BAMS-D-18-0036.1
894 Stone R.S., Dutton E.G., Harris J.M., Longenecker D., 2002. Earlier spring snowmelt in northern
895 Alaska as an indicator of climate change, *J. Geophys. Res*. **107**(D10): 4089.
896 https://doi.org/10.1029/2000JD000286
897 Stoy P.C., Mauder M., Foken T., Marcolla B., Boegh E., Ibrom A., Arain M.A., Arneth A.,
898 Aurela M., Bernhofer C., Cescatti A., Dellwik E., Duce P., Gianelle D., van Gorsel E., Kiely
899 G., Knohl A., Margolis H., McCaughey H., Merbold L., Montagnani L., Papale D.,
900 Reichstein M., Saunders M., Serrano-Ortiz P., Sottocornola M., Spano D., Vaccari F.,
901 Varlagin A., 2013. A data-driven analysis of energy balance closure across FLUXNET
902 research sites: The role of landscape scale heterogeneity. *Agric. Forest Meteorol*. **171-172**:
903 137–152. https://doi.org/10.1016/j.agrformet.2012.11.004
904 Su Z., 2002. The Surface Energy Balance System (SEBS) for estimation of turbulent heat fluxes.
905 *Hydrol. Earth Syst. Sci*. **6**(1): 85–100. https://doi.org/10.5194/hess-6-85-2002

906 Sun T., Wang Z.-H., Ni G.-H., 2013. Revisiting the hysteresis effect in surface energy budgets.
907 *Geophys. Res. Lett*. **40**(9): 1741–1747. https://doi.org/10.1002/grl.50385
908 Wilson K., Goldstein A., Falge E., Aubinet M., Baldocchi D., Berbigier P., Bernhofer C.,
909 Ceulemans R., Dolman H., Field C., Grelle A., Ibrom A., Law B.E, Kowalski A., Meyers T.,
910 Moncrieff J., Monson R., Oechel W., Tenhunen J., Valentini R., Verma S., 2002. Energy
911 balance closure at FLUXNET sites. *Agric. Forest Meteorol*. **113**(1-4): 223–243.
912 https://doi.org/10.1016/S0168-1923(02)00109-0
913 Wilczak J.M., Oncley S.P., Stage S.A., 2001. Sonic anemometer tilt correction algorithms.
914 *Boundary-Layer Meteorol.* **99**(1): 127–150. https://doi.org/10.1023/A:1018966204465
915 Wilczak J.M., Stoelinga M., Berg L., Sharp J., Draxl C., McCaffrey K., Banta R.M., Bianco L.,
916 Djalalova I., Lundquist J.K., Muradyan P., Choukulkar A., Leo L., Bonin T., Pichugina Y.,
917 Eckman R., Long C., Lantz K., Worsnop R., Bickford J., Bodini N., Chand D., Clifton A.,
918 Cline J., Cook D., Fernando H.J.S., Friedrich K., Krishnamurthy R., Marquis M., McCaa J.,
919 Olson J., Otarola-Bustos S., Scott G., Shaw W.J., Wharton S., White A.B., 2019. The second
920 Wind Forecast Improvement Project (WFIP2): Observational field campaign. *Bull. Amer.*
921 *Meteorol. Society*. **100**(9): 1701–1723. https://doi.org/10.1175/BAMS-D-18-0035.1
922 Yang K., Wang J., 2008. A temperature prediction-correction method for estimating surface soil
923 heat flux from soil temperature and moisture data. *Sci. China Ser. D: Earth Sci*. **51**(5): 721–
924 729. https://doi.org/10.1007/s11430-008-0036-1
925 Yao Y., Liang S., Li X., Chen J., Wang K., Jia K., Cheng J., Jiang B., Fisher J.B., Mu Q.,
926 Grünwald T., Bernhofer C., Roupsard O., 2015. A satellite-based hybrid algorithm to
927 determine the Priestley-Taylor parameter for global terrestrial latent heat flux estimation

928 across multiple biomes. *Remote Sens. Environ*. **165**: 216–233.
929 https://doi.org/10.1016/j.rse.2015.05.013
930
931

Table 1

The SEB closure without and with the soil heat flux G in Eq. (1) at different temporal scales for the entire dataset and separately for dry and wet soils. Soil physical composition: silt (73%), sand (14%), and clay (13%).

Averaging timescales	$(H_S + H_L)/R_{net}$			$(H_S + H_L + G)/R_{net}$		
	Entire	Dry	Wet	Entire	Dry	Wet
Half-hourly	0.763	0.786	0.715	0.946	0.983	0.922
Daily	0.852	0.915	0.794	0.948	1.000	0.908
Weekly	0.908	0.939	0.883	0.980	0.998	0.967
Monthly	0.906	1.057	0.859	0.956	0.9828	0.954
Seasonal	0.989	0.9987	0.948	1.001	1.018	0.965
Sub-annual (311 days)	1.020	N/A	N/A	0.953	N/A	N/A

941 **Figure Captions**

942

943 Fig. 1. Maps showing the WFIP 2 study area located along the Columbia River Gorge in eastern
944 Oregon and Washington states.

945

946 Fig. 2. View of the flux tower and instruments at the WFIP 2 Physics site PS01 during late
947 summer conditions (15 September 2016).

948

949 Fig. 3. Time series of (*a*) wind speed, (*b*) true wind direction, (*c*) air temperature, and (*d*) relative
950 humidity based on the half-hourly raw data for year days 176–487 (24 June 2016-01 May 2017)
951 observed at Columbia River Gorge, OR during WFIP 2 Project (Physics site PS01).

952

953 Fig. 4. Time series of (*a*) soil temperature and (*b*) soil moisture observed at the WFIP 2 Physics
954 site PS01, (*c*) rain rate observed near the Wasco State Airport, OR (WCO), and (*d*) soil types for
955 year days 176–487 (24 June 2016-01 May 2017). The data are based on half-hour averaging.

956

957 Fig. 5. Time series of (*a*) short-wave (SW) downwelling and upwelling radiation, (*b*) long-wave
958 (LW) downwelling and upwelling radiation, (*c*) SW balance, LW balance, and net radiation, and
959 (*d*) albedo for year days 176–487 (24 June 2016-01 May 2017) observed at Columbia River
960 Gorge, OR during WFIP 2 Project. The data are based on half-hour and daily averaging.

961

962 Fig. 6. Time series of (*a*) friction velocity observed at 3 and 10 m, (*b*) sensible heat flux observed
963 at 3 and 10 m, (*c*) latent heat (water vapor) flux, and (*d*) soil types for year days 176–487 (24

964 June 2016-01 May 2017) observed at Columbia River Gorge, OR during WFIP 2 Project. The
965 data are based on half-hour averaging.
966
967 Fig. 7. Scatter plots of the sum of the sensible and latent heat fluxes $H_S + H_L$ versus the net
968 radiation R_{net} based on (*a*) the half-hourly averaged (symbols) and the bin-averaged (solid line)
969 data and (*b*) the daily, monthly and 311-day (the entire dataset) averaged fluxes for the entire
970 dataset collected at Columbia River Gorge, OR during WFIP 2 Project during year days 176–487
971 (24 June 2016-01 May 2017).
972
973 Fig. 8. Plots of the bin-averaged (solid lines) and 0.5-hr averaged (symbols) turbulent fluxes
974 (eddy-covariance) of (*a*) sensible heat H_S, (*b*) latent heat H_L, and (c) the sum $H_S + H_L$ (SEB
975 turbulent flux components) versus the net radiation R_{net} for dry, wet, and frozen soils observed
976 at Columbia River Gorge, OR during WFIP 2 Project during year days 176–487 (24 June 2016-
977 01 May 2017).
978
979 Fig. 9. Plots of the sum of the sensible and latent heat fluxes $H_S + H_L$ versus the net radiation
980 R_{net} separately for (*a*) dry, (*b*) wet, and (*c*) frozen (snow covered) soils based on daily averaged
981 fluxes and entire dataset averaging (81, 92, and 58-day averaging in each case respectively).
982
983 Fig. 10. One-month (30-day) time series of (*a*) the net radiation R_{net}, (*b*) the sum of the sensible
984 and latent heat fluxes $H_S + H_L$, (*c*) the residual energy $R_{net} - H_S - H_L$ and (*d*) difference of the
985 soil temperature between 10 cm and 5 cm levels for dry soils observed at the WFIP 2 Physics site

PS01 during year days 240–270 (27 August-26 September 2016). The data are based on half-hour and daily averaging.

Fig. 11. Same as Fig. 10 but for wet soils observed at the WFIP 2 Physics site PS01 during year days 450–480 (25 March-24 April 2017). The data are based on half-hour and daily averaging.

Fig. 12. Same as Fig. 10 but for frozen (snow covered) soils observed at the WFIP 2 Physics site PS01 during year days 395–425 (29 January-28 February 2017). The data are based on half-hour and daily averaging.

Fig. 13. The incomplete SEB closure equation (without the ground heat flux G) at different temporal scales: ratio of turbulent energy fluxes $H_S + H_L$ to net radiation R_{net} for the entire dataset (red solid line and red symbols) and separately for different soil types (dry, wet, and frozen) plotted versus averaging time based on the data collected at Columbia River Gorge, OR during WFIP 2 Project.

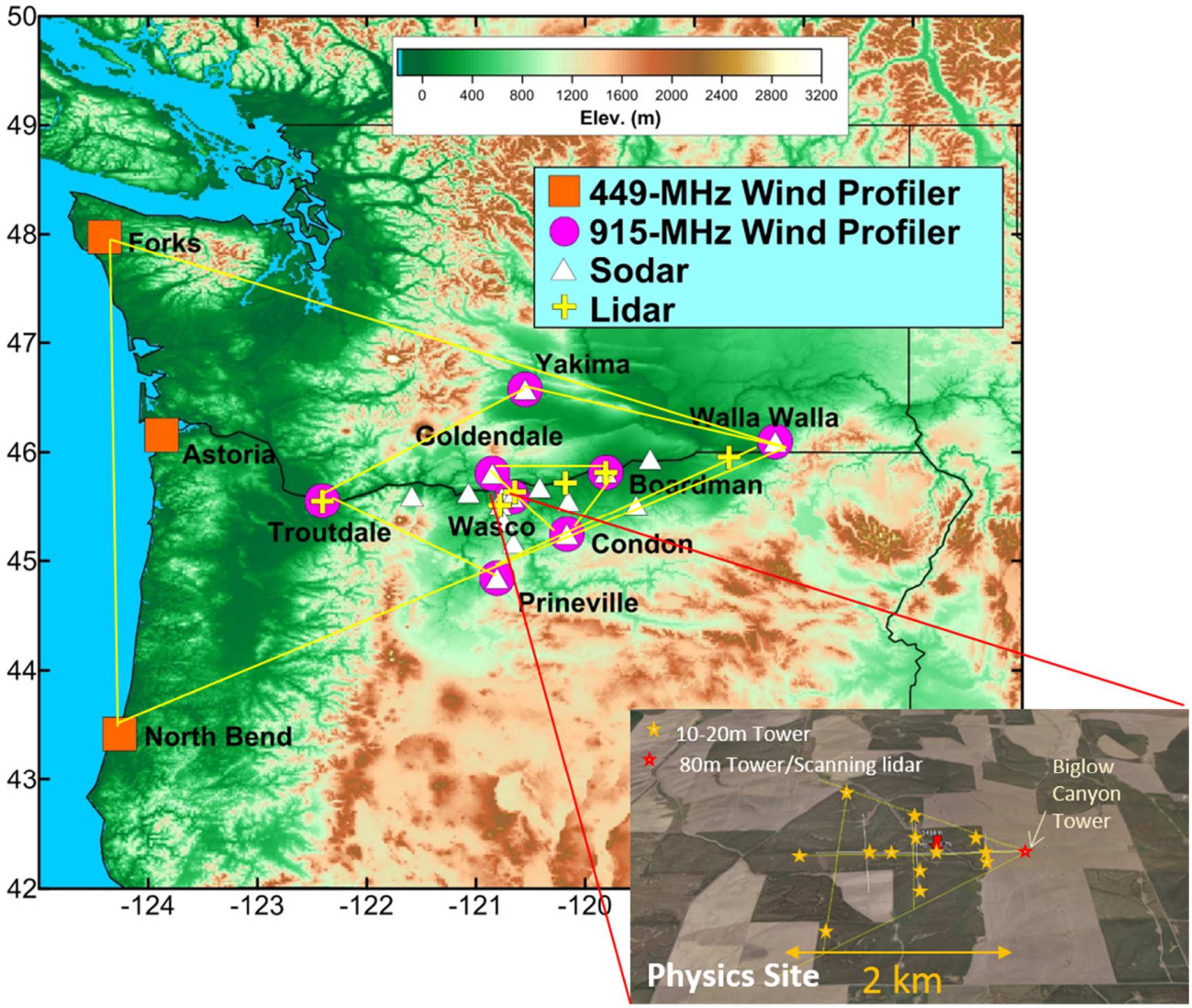

Fig. 1. Maps showing the WFIP 2 study area located along the Columbia River Gorge in eastern Oregon and Washington states.

Fig. 2. View of the flux tower and instruments at the WFIP 2 Physics site PS01 during late summer conditions (15 September 2016).

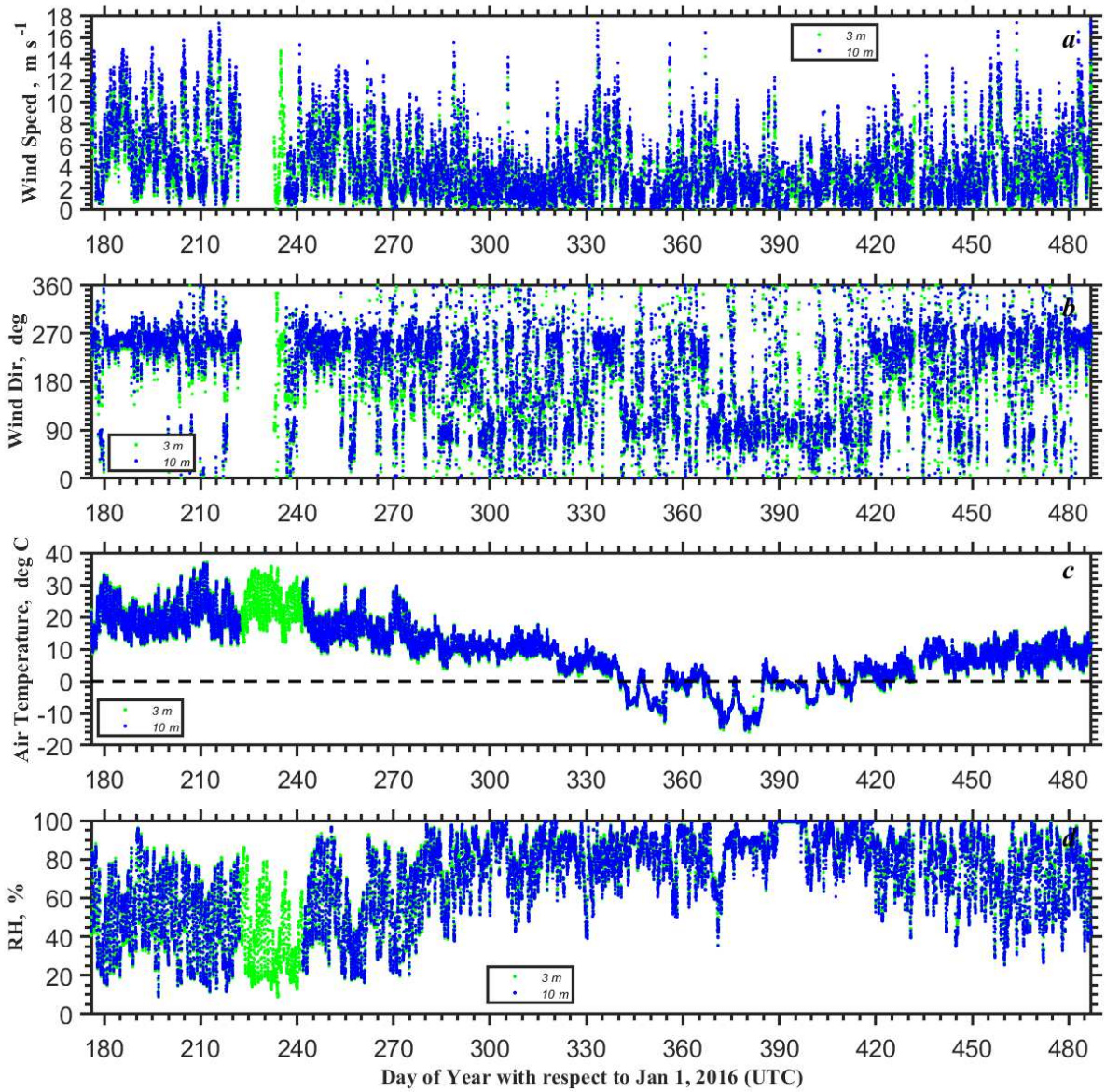

1017

1018 **Fig. 3.** Time series of (*a*) wind speed, (*b*) true wind direction, (*c*) air temperature, and (*d*) relative

1019 humidity based on the half-hourly raw data for year days 176–487 (24 June 2016-01 May 2017)

1020 observed at Columbia River Gorge, OR during WFIP 2 Project (Physics site PS01).

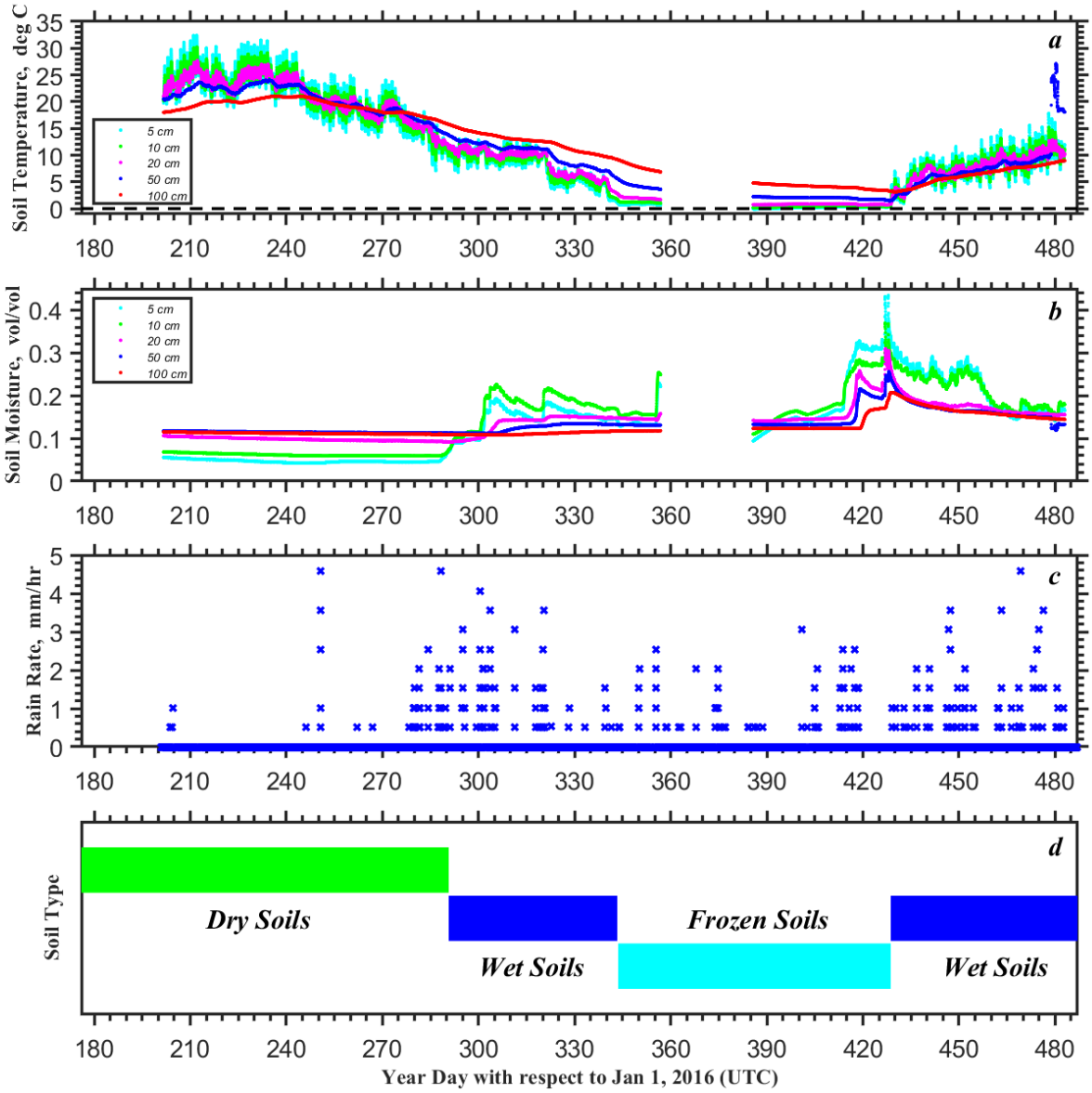

1021

1022 **Fig. 4.** Time series of (*a*) soil temperature and (*b*) soil moisture observed at the WFIP 2 Physics

1023 site PS01, (*c*) rain rate observed near the Wasco State Airport, OR (WCO), and (*d*) soil types for

1024 year days 176–487 (24 June 2016-01 May 2017). The data are based on half-hour averaging.

1025

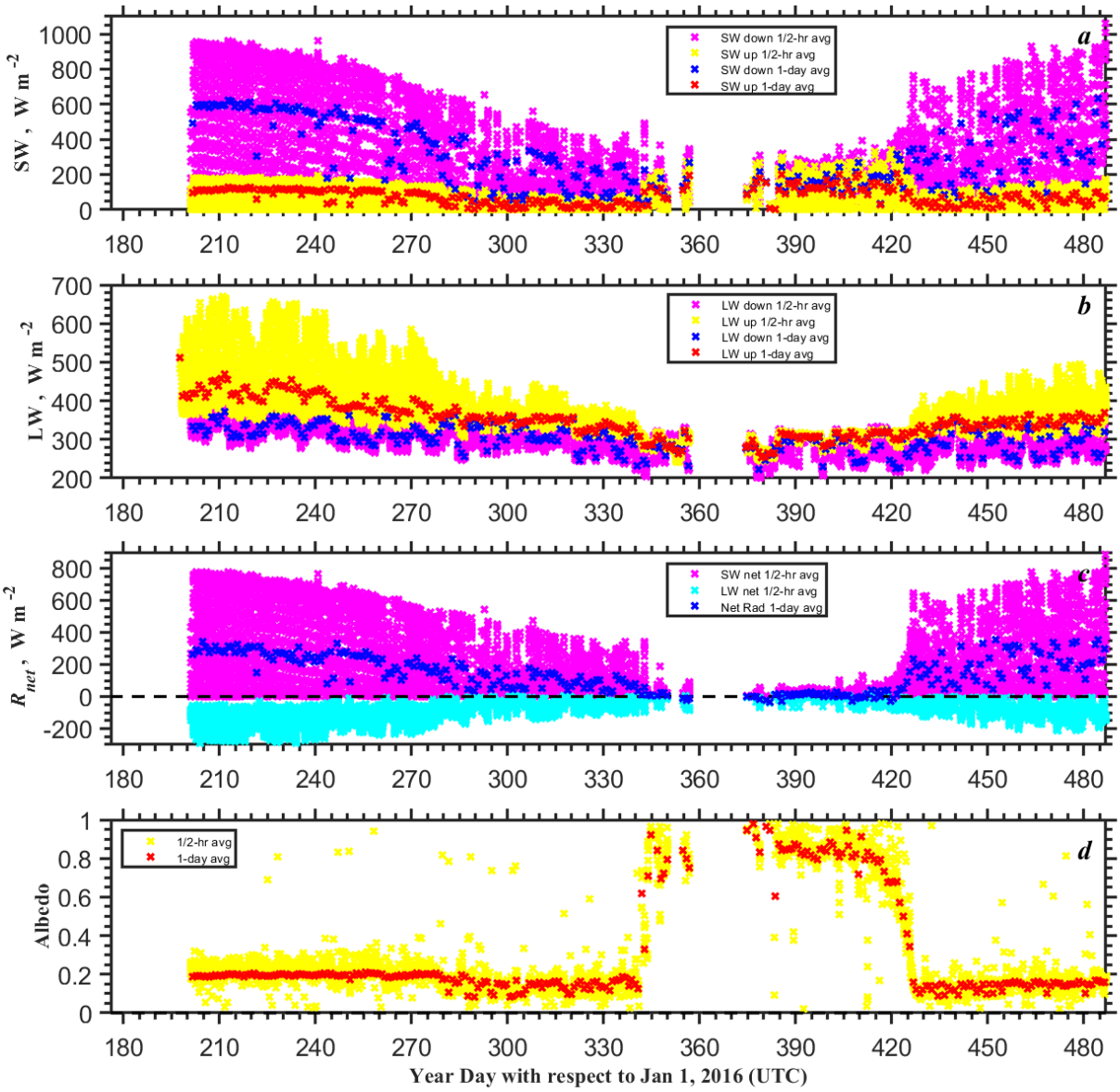

Fig. 5. Time series of (*a*) short-wave (SW) downwelling and upwelling radiation, (*b*) long-wave (LW) downwelling and upwelling radiation, (*c*) SW balance, LW balance, and net radiation, and (*d*) albedo for year days 176–487 (24 June 2016-01 May 2017) observed at Columbia River Gorge, OR during WFIP 2 Project. The data are based on half-hour and daily averaging.

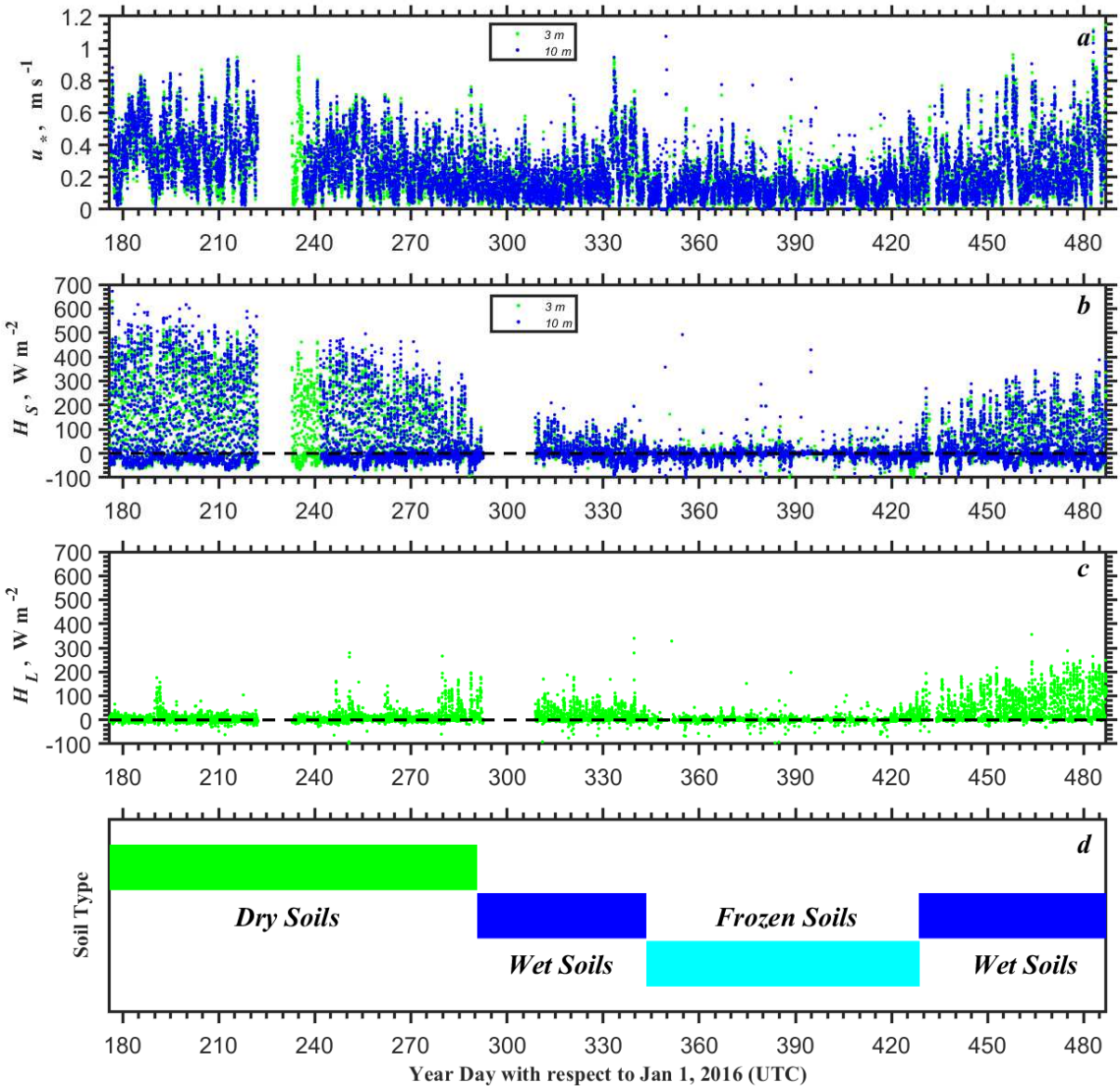

1031

1032 **Fig. 6.** Time series of (*a*) friction velocity observed at 3 and 10 m, (*b*) sensible heat flux

1033 observed at 3 and 10 m, (*c*) latent heat (water vapor) flux, and (*d*) soil types for year days 176–

1034 487 (24 June 2016-01 May 2017) observed at Columbia River Gorge, OR during WFIP 2

1035 Project. The data are based on half-hour averaging.

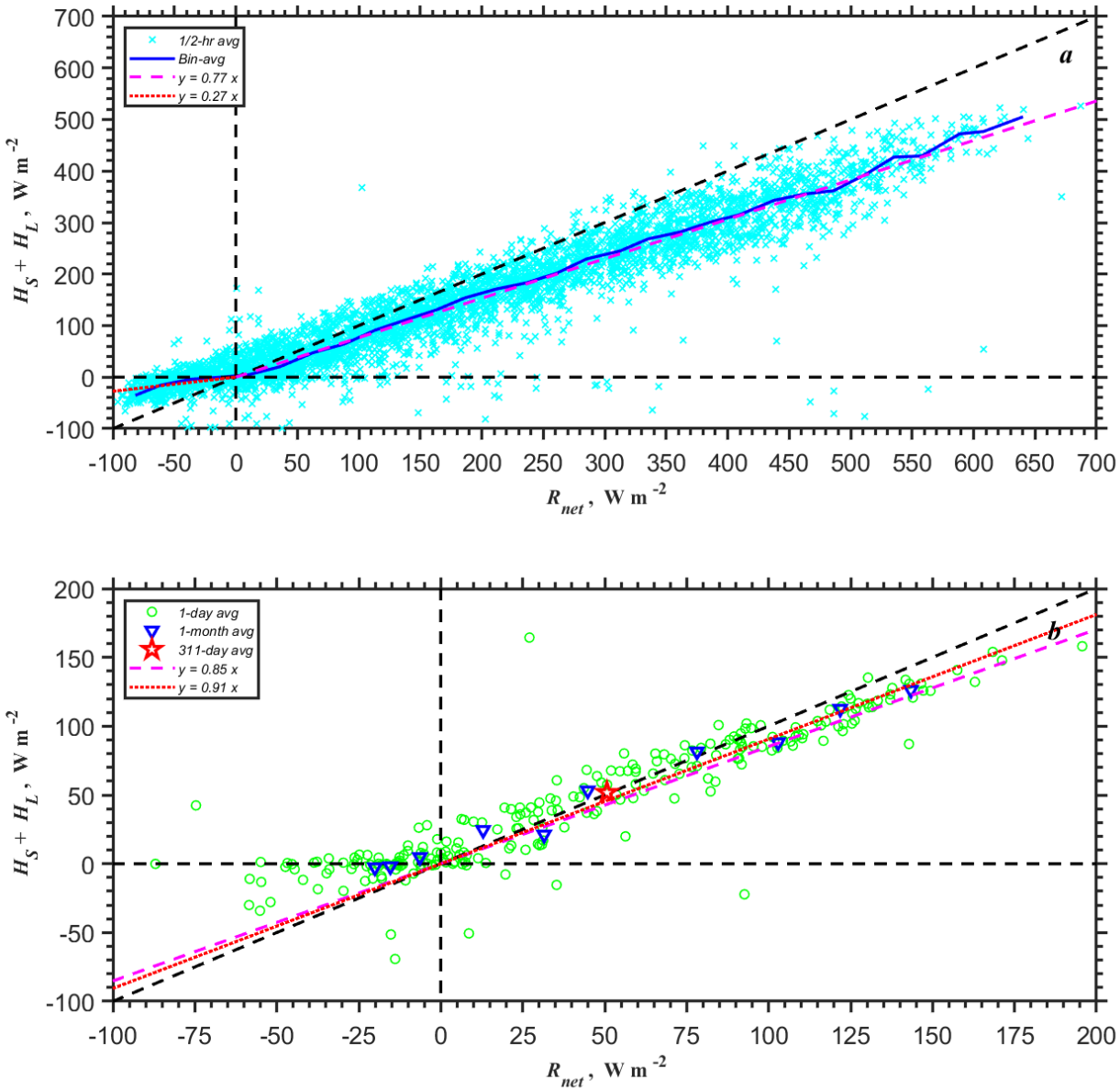

Fig. 7. Scatter plots of the sum of the sensible and latent heat fluxes $H_S + H_L$ versus the net radiation R_{net} based on (*a*) the half-hourly averaged (symbols) and the bin-averaged (solid line) data and (*b*) the daily, monthly and 311-day (the entire dataset) averaged fluxes for the entire dataset collected at Columbia River Gorge, OR during WFIP 2 Project during year days 176–487 (24 June 2016-01 May 2017).

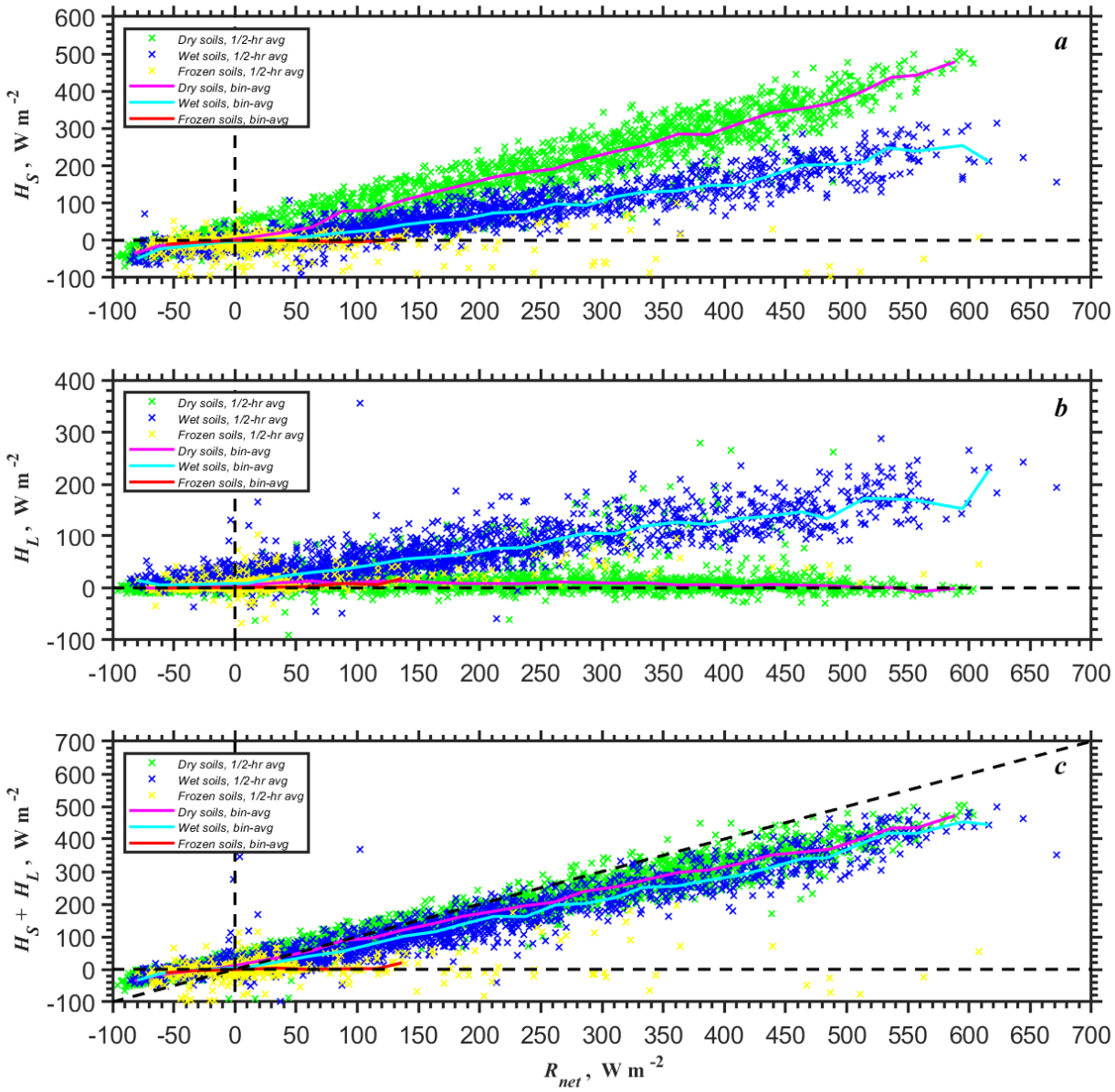

1043

1044 **Fig. 8.** Plots of the bin-averaged (solid lines) and 0.5-hr averaged (symbols) turbulent fluxes
1045 (eddy-covariance) of (*a*) sensible heat H_S, (*b*) latent heat H_L, and (c) the sum $H_S + H_L$ (SEB
1046 turbulent flux components) versus the net radiation R_{net} for dry, wet, and frozen soils observed
1047 at Columbia River Gorge, OR during WFIP 2 Project during year days 176–487 (24 June 2016-
1048 01 May 2017).
1049

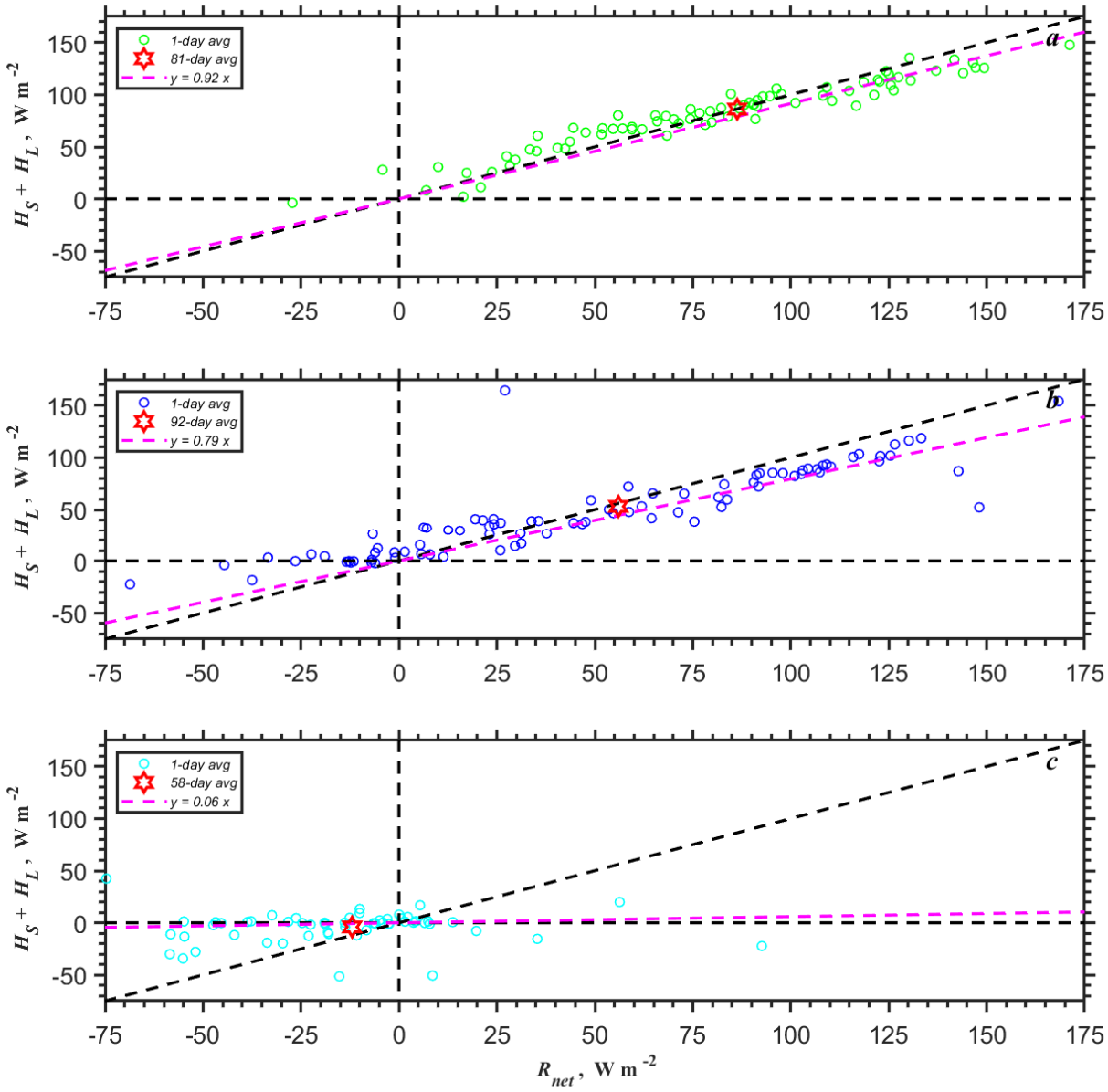

1050

1051 **Fig. 9.** Plots of the sum of the sensible and latent heat fluxes $H_S + H_L$ versus the net radiation
1052 R_{net} separately for (*a*) dry, (*b*) wet, and (*c*) frozen (snow covered) soils based on daily averaged
1053 fluxes and entire dataset averaging (81, 92, and 58-day averaging in each case respectively).

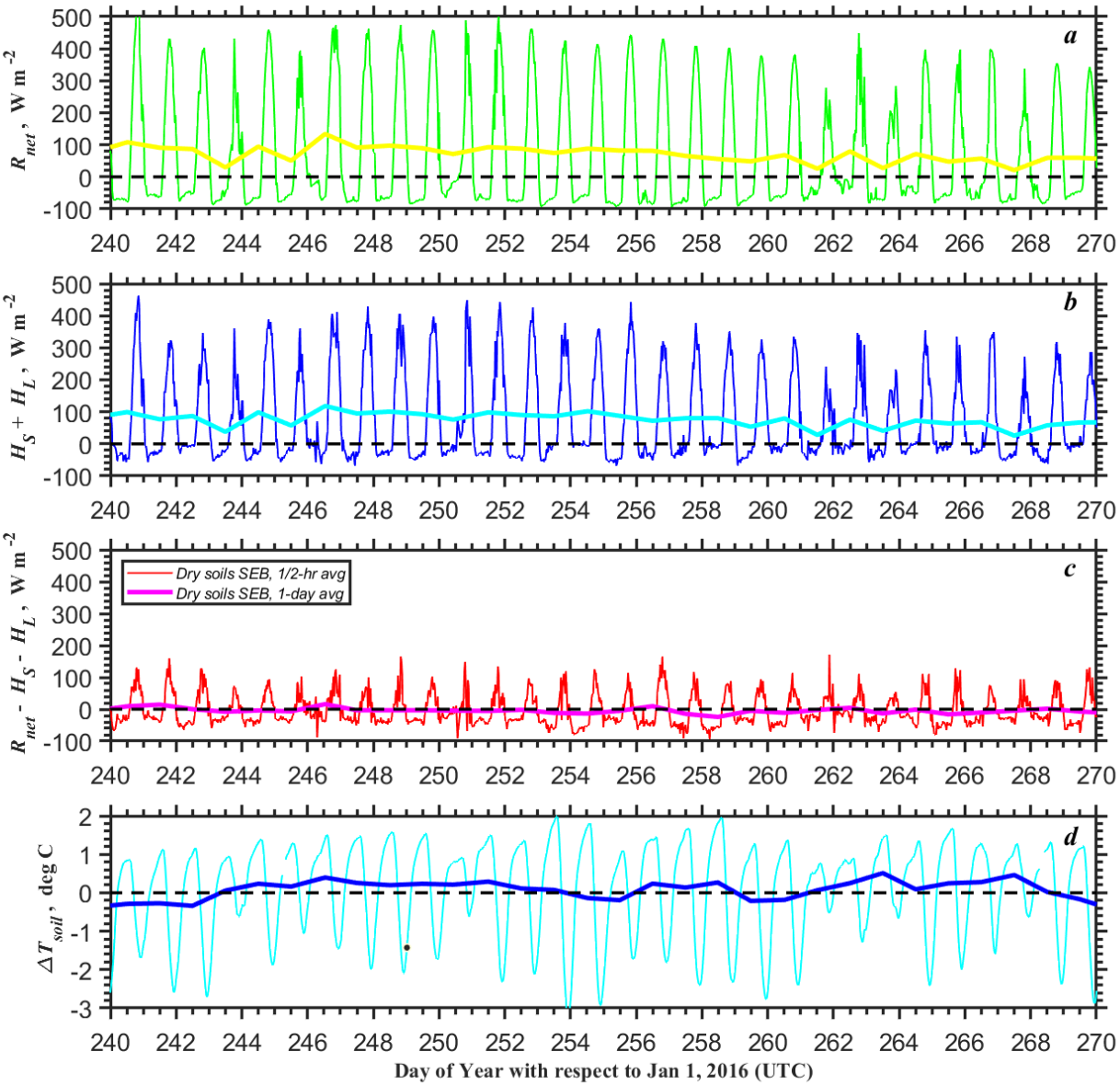

1054

1055 **Fig. 10.** One-month (30-day) time series of (*a*) the net radiation R_{net}, (*b*) the sum of the sensible
1056 and latent heat fluxes $H_S + H_L$, (*c*) the residual energy $R_{net} - H_S - H_L$ and (*d*) difference of the
1057 soil temperature between 10 cm and 5 cm levels for dry soils observed at the WFIP 2 Physics site
1058 PS01 during year days 240–270 (27 August-26 September 2016). The data are based on half-
1059 hour and daily averaging.

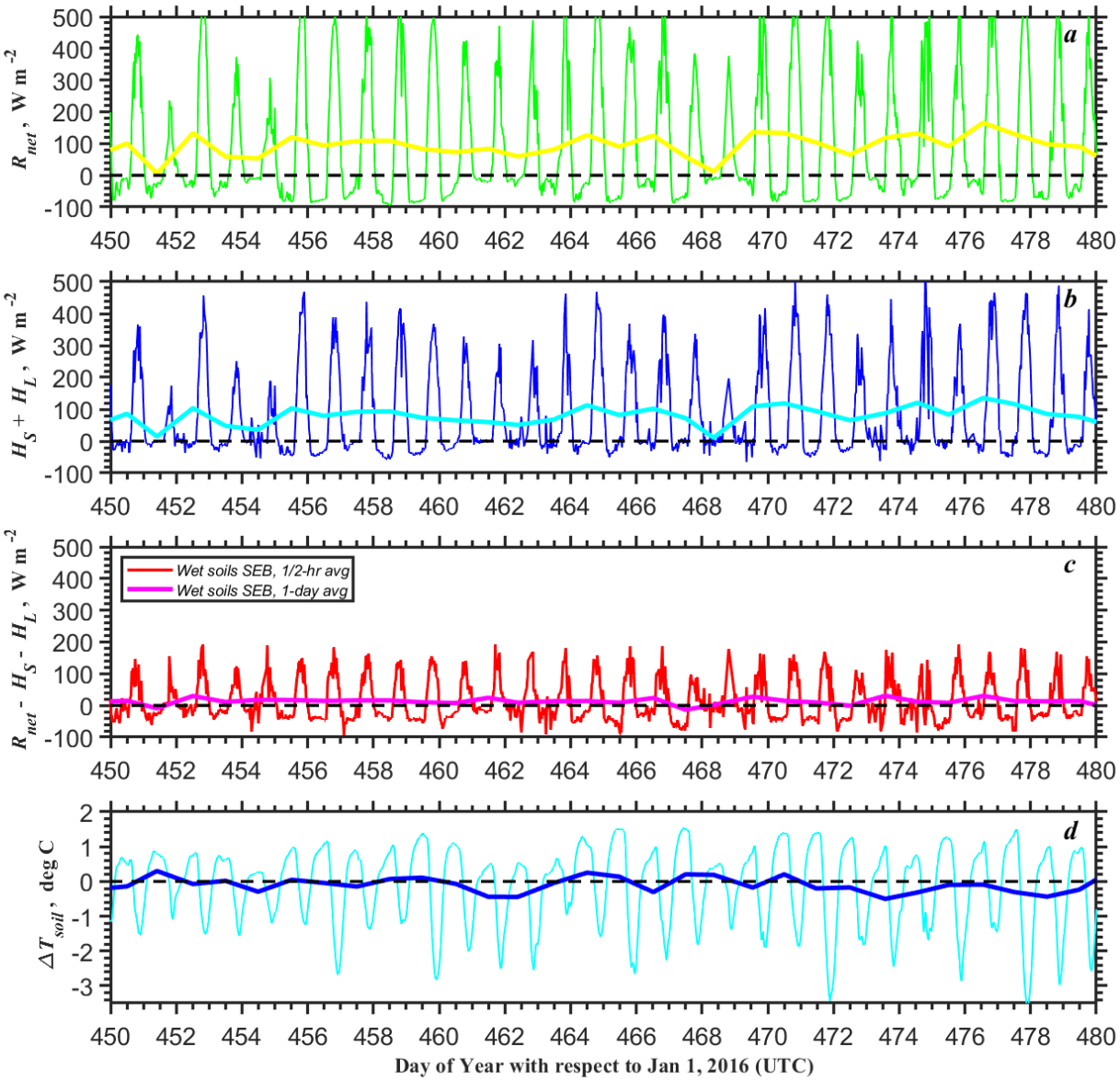

1060

1061 **Fig. 11.** Same as Fig. 10 but for wet soils observed at the WFIP 2 Physics site PS01 during year

1062 days 450–480 (25 March-24 April 2017). The data are based on half-hour and daily averaging.

1063

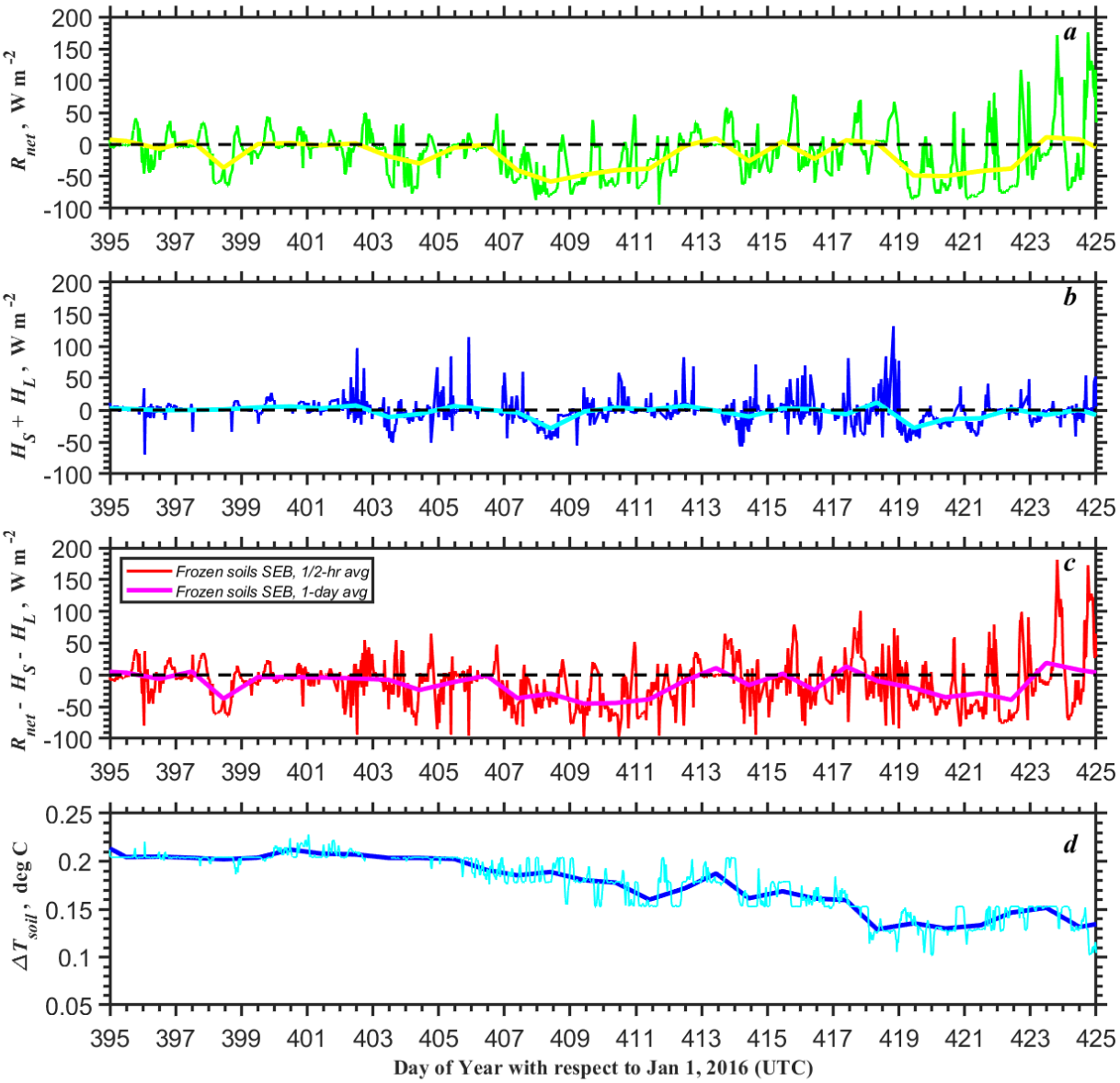

1064

1065 **Fig. 12.** Same as Fig. 10 but for frozen (snow covered) soils observed at the WFIP 2 Physics site

1066 PS01 during year days 395–425 (29 January-28 February 2017). The data are based on half-hour

1067 and daily averaging.

1068

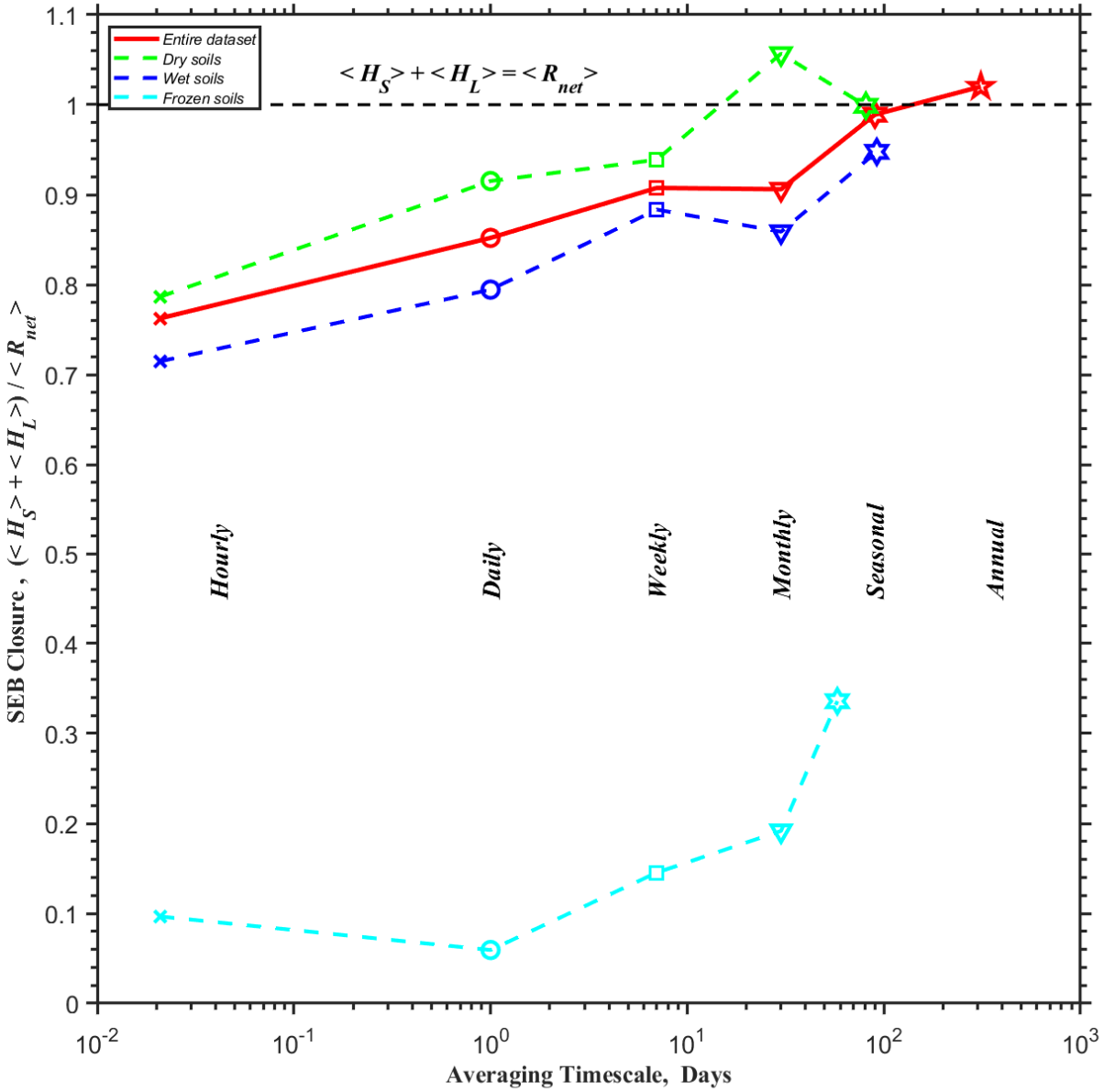

1069

1070 **Fig. 13.** The incomplete SEB closure equation (without the ground heat flux G) at different
1071 temporal scales: ratio of turbulent energy fluxes $H_S + H_L$ to net radiation R_{net} for the entire
1072 dataset (red solid line and red symbols) and separately for different soil types (dry, wet, and
1073 frozen) plotted versus averaging time based on the data collected at Columbia River Gorge, OR
1074 during WFIP 2 Project.